Liu Tianshu (Orcid ID: 0000-0001-6297-1660)
Sayanagi Kunio, M. (Orcid ID: 0000-0001-8729-0992)
Blalock John, J (Orcid ID: 0000-0002-7460-1074)
Ingersoll Andrew (Orcid ID: 0000-0002-2035-9198)
Ewald Shawn, P (Orcid ID: 0000-0002-1567-9154)

Saturn's north polar vortex structure extracted from cloud images by the optical flow method

Tianshu Liu[1], Kunio M. Sayanagi[2], Shawn R. Brueshaber[1], John J. Blalock[2]

Andrew P. Ingersoll[3], Ulyana A. Dyudina[3], Shawn P. Ewald[3]

1: Department of Mechanical and Aerospace Engineering

Western Michigan University, Kalamazoo, MI 49008, USA

Email: tianshu.liu@wmich.edu, Telephone: 269-323-2814

2: Department of Atmospheric and Planetary Sciences

Hampton University, Hampton, VA 29668

3: Division of Geological and Planetary Sciences

California Institute of Technology, Pasadena, CA, 91125, USA

(Final version for Journal of Geophysical Research: Planets

for consideration of publication as a research article)

(09/23/2019)

Abstract

The paper presents velocity fields with ~3-km spatial resolution of Saturn's north polar vortex (NPV) retrieved using the optical flow method from a sequence of polar-projected cloud images captured by the Imaging Science Subsystem camera on board NASA's Cassini spacecraft. The fields of the velocity magnitude, velocity variation, relative vorticity, divergence and second invariant are determined to characterize the flow structures of the inner core of the NPV. The mean zonal and mean meridional velocity profiles of the NPV are compared with previous measurements. We also describe the relevant details of application of the optical flow method to planetary cloud tracking wind measurements. The mean zonal velocity profile is consistent with the previous measurements using correlation image velocimetry methods. The small but significant meridional velocity corresponds to outwardly spiraling streams observed in the region near the north pole (NP). The concentrated vorticity and second invariant within 1-degree planetographic latitude of the NP indicate strong rotational motion of the fluid. An analysis is presented to explore a possible physical origin of the observed spiraling node at the NP.

Plain Language Summary

A swirling flow pattern with wind speeds peaking at about 100 m s^{-1} was revealed in Saturn's North Polar Vortex (NPV) in high-resolution images captured by the Imaging Science Subsystem camera on board NASA's Cassini spacecraft in November 2012. Using sequences of images that show clouds in the NPV, the motions of these clouds were analyzed to measure the wind speeds in the north-polar region. The high-precision wind measurements presented in the current report are enabled by the optical flow cloud tracking method. The time-averaged wind field shows a well-defined counter-clockwise (cyclonic) vortex at the pole. In particular, the observed flow structures and wind shear near the pole indicate strong rotational motion of the north polar atmosphere with upwelling at the center.

1. Introduction

The atmospheric flow structures near Saturn's north and south poles (NP and SP) have attracted considerable attention in the scientific community and public (Godfrey 1988; Sánchez-Lavega et al. 2006; Baines et al. 20I7, 2009; Fletcher et al. 2008; Dyudina et al. 2009, Sayanagi et al. 2018; Studwell et al. 2018). In particular, recent studies have been focused on the stable cyclonic vortex centered at the north pole (hereafter referred to as NPV), which extends from 85°N to the north pole with zonal winds of order of about 100 m s^{-1} (Antunano et al. 2015, 2018; Sayanagi et al. 2017). Prior studies reported zonal and meridional wind profiles as well as vorticity and divergence fields of the NPV, which had been measured using images of Saturn obtained during different orbits of the Cassini spacecraft. The observed structure of the NPV did not significantly change between different epochs. However, prior studies using the conventional Correlation Imaging Velocimetry (CIV) methods have many gaps in their velocity measurements in areas where no trackable features were detected (Sayanagi et al. 2017). The current study re-analyzes the images previously analyzed by Sayanagi et al. (2017) using the optical flow method to retrieve the velocity field of the NPV at a significantly higher spatial resolution.

To place the optical flow method in context, a review of existing cloud tracking methods used in the planetary sciences is provided below. The idea to track clouds to measure motions on a planetary surface has been applied since Hooke (1665) made the first telescopic observations of Jupiter and measured the motion for what may have been the Great Red Spot (GRS). The beginning of planetary mission-based imaging science campaigns dramatically increased the number of features that can be tracked, and various methods have been developed to deduce winds from the motion of trackable features. Manual tracking is the simplest method which relies on human's innate sense of pattern recognition. A human operator visually inspects a sequence of cloud maps, identifies common clouds displayed in

sequence, and marks their coordinates. A pair of coordinates that marks the locations of a common cloud (called *tie points*) is converted to a wind vector by dividing the displacement by a time interval. The strength of the manual tracking method is the high confidence of returned vectors with very few spurious tie-point matches, but it is a labor-intensive process that returns relatively few tie points. This method has been used in determining long-term trends in zonal winds of Jupiter using Voyager, HST, Galileo and Cassini data (Mitchell et al. 1981; Dowling and Ingersoll 1988; Sada et al. 1996; Vasavada et al. 1998; Simon-Miller et al. 2002, 2006, 2007, 2010; Sanchez-Lavega et al. 2000; Cheng et al. 2008).

The one-dimensional correlation method is the simplest of the automated cloud-tracking wind measurement methods. This method takes a latitudinal scan of cloud brightness from two overlapping cloud maps, and searches for a longitudinal shift that maximizes the correlation between the two scans. The displacement that maximizes the correlation is then converted to zonal wind speed. A major advantage of this method is that it works for images with a relatively poor contrast; however, it measures only zonal-mean zonal-wind profile and does not yield a wind field map. This method has been used by Limaye (1986) to calculate Jupiter's zonal wind profile from Voyager data, Garcia-Melendo and Sanchez-Lavega (2001) to study the long-term trends in Jupiter's zonal wind profile using HST data, and Sayanagi et al (2013) to detect zonal wind speed change caused by a giant storm on Saturn.

Correlation imaging velocimetry (CIV) is an automated method that produces tie-point vectors from a pair of mapped images by calculating the two-dimensional correlation coefficient as a function of the displacement from a given point. The displacement vector that maximizes the correlation between a window in the first image and a displaced window in the second image is determined to be a tie-point match. This method can be enhanced such that it first performs a coarse-search followed by a refined-search (Choi et al. 2008, 2010, Kouyama et al. 2012) by using a human operator to perform quality control (Hueso et al.

2009), and by averaging along streamlines found in the derived wind field to smooth the flow field (Sussman et al. 2010). The strength of CIV method is its ability to automatically generate a large number of regularly-spaced tie-points. However, it is challenging to identify and eliminate spurious tie-point matches. CIV has been used to derive wind fields on Venus using Galileo and Venus Express data (Kouyama et al 2012, 2013), Jupiter's Great Red Spot using Galileo images (Choi et al. 2007), Oval BA using Galileo, Cassini and New Horizon images (Hueso et al. 2009, Choi et al. 2010), and Saturn using Cassini images (Sayanagi et al. 2011).

A more advanced cloud tracking method incorporating fluid-dynamic corrections to CIV methods is the Advection Corrected Correlation Imaging Velocimetry (ACCIV) method developed at University of California Berkeley (Asay-Davis et al. 2009). The first step in this method makes an estimate of a flow field using a simple CIV method from a pair of cloud maps. It then uses the estimated flow field to forward-advect the clouds in the first image to be compared to the second image. The difference between the advected first image and the second image is used as a correction to the wind field, and the process is iterated until the wind field reaches a satisfactory convergence. In addition, the iteration can also involve backward propagation of the second image to be compared to the unaltered first image. The ACCIV has been used to analyze Oval BA (Asay-Davis et al. 2009), giving high-resolution wind fields.

The optical flow method used in the current study is developed by projecting the three-dimensional transport equation onto the two-dimensional image plane (Liu and Shen 2008). Thus, in the optical flow method, the 3D partial differential equation (PDE) is reduced to a 2D PDE called the optical flow equation in the image plane, where the physical significance and mathematical definition of the optical flow are given (see Section 2). In contrast to the correlation-based methods, the variational optical flow method is a differential method that

seeks a numerical solution to the optical flow equation to determine the displacement vectors of cloud patterns between a pair of images. The optical flow method is particularly suitable for extraction of small displacements from continuous patterns (such as cloud patterns) at a spatial resolution of one vector per pixel.

In this work, the optical flow method is applied to a sequence of fourteen polar-projected images of Saturn's north pole, which was captured by the Narrow-Angle Camera (NAC) on board the Cassini spacecraft over a period of 5 hours and 19 min. on November 27, 2012. The same image sequence was previously analyzed by Sayanagi et al. (2017). The interval between consecutive images varies from 20.5 min to 29.1 min. Figure 1 shows the first four of the 14 NPV images analyzed in the current paper.

The application of the optical flow method for planetary cloud tracking measurements is presented in Section 2. To determine the optical flow as an inverse problem, the Euler-Lagrange equation is derived using a variational method with a smoothness constraint applied. Selection of the relevant parameters in optical flow computation is discussed, and the accuracy of the optical flow method applied to Saturn's NPV images is evaluated through simulations. In Section 3, the processes to prepare the images for the analysis in the current study are described, and the extracted flow structures of the NPV are discussed. Finally, the conclusions are given in Section 4.

2. Optical flow method for cloud tracking

2.1. Variational method for determining the optical flow

The derivation of the optical flow equation from the relevant governing equations in fluid mechanics for various flow visualization images is presented in Liu and Shen (2008). For motion of light-scattering particles (cloud aerosols in this case), the governing equation is the disperse phase number equation, $\partial N_p / \partial t + \nabla \cdot \left(N_p \boldsymbol{U} \right) = 0$, where $\boldsymbol{U} = \left(U_1, U_2, U_3 \right)$ is the

particle velocity in a three-dimensional (3D) object (physical) space and N_p is the number of particles per unit total volume. By evaluating the light scattering process through flow containing light-scattering particles, the optical flow equation in the image plane can be derived. The optical flow equation is written as

$$\partial I_N / \partial t + \nabla \cdot \left(I_N \boldsymbol{u} \right) = F\left(x_1, x_2 \right), \tag{1}$$

where $\boldsymbol{u}$ is the optical flow (i.e., the 3D flow projected onto the image plane), $\nabla = \partial / \partial x_i$ $(i = 1,2)$ is a gradient operator in the image plane, and the boundary term $F = w_{ext} \left\langle C_{ext} \right\rangle_a \boldsymbol{n} \cdot \left(N_p \boldsymbol{U} \right) \Big|_{\Gamma_1}^{\Gamma_2}$ acts as a source/sink term representing the effect of particles accumulated within a cloud layer confined by two control planes Γ_1 and Γ_2. The planes Γ_1 and Γ_2 approximate the top and bottom of a cloud layer, respectively. In Eq. (1), the normalized image intensity $I_N = \Delta I / I_0$ is an input, which is proportional to the normalized radiance $L_N = \left(L^- \left(\tau_H \right) - L^- \left(0 \right) \right) / \left(Q_{sca} \left(0 \right) - L^- \left(0 \right) \right)$, where $L^- \left(\tau_H \right)$ and $L^- \left(0 \right)$ are the radiances scattered from particles toward a camera from Γ_1 and Γ_2, respectively, and $Q_{sca} \left(0 \right)$ is a scattering source term at Γ_1. The image intensities ΔI and I_0 are proportional to $L^- \left(\tau_H \right) - L^- \left(0 \right)$ and $Q_{sca} \left(0 \right) - L^- \left(0 \right)$, respectively. Here, τ_H is the optical depth of the distance H between Γ_1 and Γ_2 along a light ray, which is defined as $\tau_H = \int_{\Gamma_1}^{\Gamma_2} \beta \, ds$, where β is an extinction coefficient of particles.

The optical flow in Eq. (1) is represented as $\boldsymbol{u} = \left(u_1, u_2 \right) = \gamma \left\langle \boldsymbol{U}_{12} \right\rangle_N$, where $\left\langle \boldsymbol{U}_{12} \right\rangle_N$ is the light-path-averaged particle velocity defined as

$$\left\langle \boldsymbol{U}_{12} \right\rangle_N = \frac{\int_{\Gamma_1}^{\Gamma_2} N_p \boldsymbol{U}_{12} \, dX_3}{\int_{\Gamma_1}^{\Gamma_2} N_p \, dX_3}, \tag{2}$$

$\boldsymbol{U}_{12} = (U_1, U_2)$ is the velocity vector parallel to the image plane, and γ is a constant scaling factor in the orthographical projection transformation from the 3D object space onto the image plane. Therefore, physically, the optical flow represents the light-path-averaged velocity of particles. The zero-net-flux condition, i.e., $\boldsymbol{n} \cdot \left(N_p \boldsymbol{U} \right) \Big|_{\Gamma_1}^{\Gamma_2} = 0$ is assumed. Note that for a divergence-free optical flow (i.e. $\nabla \cdot \boldsymbol{u} = 0$), Eq. (1) is reduced to the Horn-Schunck's brightness constraint equation $\partial I_N / \partial t + \boldsymbol{u} \cdot \nabla I_N = 0$ (Horn and Schunck 1981). Nevertheless, the optical flow is not divergence-free generally. Thus, an inverse solution of Eq. (1) for the optical flow is not divergence-free in this work.

For a given pair of map-projected images that show moving clouds, the normalized image intensity I_N is a measurable quantity, and the objective here is to determine the optical flow $\boldsymbol{u}$. Since a single equation, Eq. (1), must be solved for two components of $\boldsymbol{u}$, this is an ill-posed problem. To solve for the optical flow as an inverse problem, a variational formulation with a smoothness constraint is used (Horn and Schunck 1981; Liu and Shen 2008; Heitz et al. 2010; Wang et al. 2015). Given I_N and F, we define a functional

$$J(\boldsymbol{u}) = \int_D \left(\partial I_N / \partial t + \nabla \cdot (I_N \boldsymbol{u}) - F \right)^2 dx_1 dx_2 + \alpha \int_D \left(|\nabla u_1|^2 + |\nabla u_2|^2 \right) dx_1 dx_2 , \quad (3)$$

where the first integral term is a equation functional, the second integral term is a first-order Tikhonov regularization functional, D is an image domain of interest, and α is a Lagrange multiplier.

Minimization of the functional $J(\boldsymbol{u})$ leads to the Euler-Lagrange equation

$$I_N \nabla \left[\partial I_N / \partial t + \nabla \cdot (I_N \boldsymbol{u}) - F \right] + \alpha \nabla^2 \boldsymbol{u} = 0 , \quad (4)$$

where $\nabla^2 = \partial^2 / \partial x_i \partial x_i$ $(i = 1,2)$ is the Laplace operator, and α is a Lagrange multiplier. When a pair of temporally separated images is given and F is neglected in a first-order approximation, a standard finite difference method can be used to solve Eq. (4) with the

Neumann condition $\partial \boldsymbol{u} / \partial n = 0$ on the image domain boundary ∂D for the optical flow $\boldsymbol{u}$. In principle, this differential method is particularly suitable for extracting high-resolution velocity fields from cloud images captured through planetary remote sensing observation. However, in reality, the effective spatial resolution is tuned by a Lagrange multiplier that essentially acts as a diffusion coefficient in Eq. (4). A larger value of a Lagrange multiplier tends to smooth out finer features. Detailed discussions of applications of the optical flow method to cloud tracking are given by Liu et al. (2012) and Liu (2014).

The optical flow algorithm used in the current work applies a Horn-Schunck estimator for an initial solution (Horn and Schunck 1981) and applies a Liu-Shen estimator for a refined solution (Wang et al. 2015; Liu 2017). Section 2.2 demonstrates that optical flow solutions do not strongly depend on a Lagrange multiplier. In this work, we use the Lagrange multiplier values of 20 and 2,000 for the Horn-Schunck and Liu-Shen estimators, respectively. Other relevant parameters are the number of iterations in successive improvement of the optical flow solution, and the sizes of the Gaussian filters to compensate for the artifacts introduced by illumination variation and noise. Liu et al. (2015) discusses how to tune the Gaussian filter sizes. As described by Sayanagi et al. (2017), the images of Saturn's NPV used in this study are corrected for illumination variation assuming Minnaert scattering; the Gaussian filter is needed to smooth the imperfections in the Minnaert scattering correction. For extraction of large displacements in the image plane, a coarse-to-fine scheme is applied to reduce the error in optical flow computation (Liu 2017). Here, a coarse-grained velocity field is initially determined from downsampled images (the image size is 1/4 of the original size in this case) and then a refined velocity field with the original spatial resolution is extracted in two iterations.

2.2. Accuracy

This subsection presents a procedure to evaluate the accuracy of the optical flow method applied to Saturn's NPV images and the effects of the selected parameters in solving the optical flow equation. The main parameters that affect optical flow computation are the Lagrange multipliers in the Horn-Schunck estimator for an initial solution and the Liu-Shen estimator for a refined solution of Eq. (4). Other relevant diagnostic parameters are the number of iterations in successive improvement of optical flow solution (computed with a coarse-to-fine iterative scheme), and the sizes of the Gaussian spatial filters. To evaluate the accuracy of optical flow solution, simulations are conducted based on a sequence of synthetic images for a given velocity field. Since the synthetic velocity field represents a known truth, direct comparison between extracted and true velocity fields allows estimation of an absolute velocity error.

Figure 2 shows clean and noisy cloud images ($1024\,pix \times 1024\,pix$) of the NPV in which cloud patterns are passively advected with simulated wind. The clean image does not use added noise, whereas the noisy image uses added Gaussian noise. A synthetic vortex velocity field is reconstructed by using the circumferential and radial velocity distributions given by $u_c = (\Gamma / 2\pi)(r+\delta)^{-1}\left(1 - exp\left(-r^2 / r_0^2\right)\right)$ and $u_r = a(r - r_0)$, where r is the radial coordinate, r_0 is a constant controlling the size of a vortex, Γ and a are constant parameters for the strength of a vortex, and δ is a small positive constant to remove the singularity at $r = 0$. This flow is a modified form of the Burgers vortex (Wu et al. 2006). The predetermined (i.e, "known truth") velocity vectors and streamlines are shown in Figs. (3a) and (4a), respectively, where the parameters controlling the vortex structure are $\Gamma = -10^4$, $a = -0.02$, $r_0 = 150$ and $\delta = 2$. Thirteen pairs of synthetic images are generated based on the first thirteen real cloud images of the NPV. In these synthetic images, flow

diverges outward from the vortex center, while flow in the outer region converges inwardly. The converging and diverging regions are segmented by a circle marked in Figs. 3-4, which is known as a stable limit cycle to which neighboring trajectories (streamlines) converge (Hurewicz 2002).

From the thirteen pairs of clean synthetic images, instantaneous velocity fields are computed using the optical flow method. Figures 3(b) and 4(b) show extracted velocity vectors and streamlines, where the presented data are downsampled for clear illustration. The averaged velocity field is calculated from 13 synthetic image pairs. Figure 4 shows that the retrieved velocity field differs minimally from the "truth." In retrieving the velocity vectors, the Lagrange multiplier in the Horn-Schunck estimator is fixed at 20, and the Lagrange multiplier in the Liu-Shen estimator is fixed at 2,000. It is found that the Liu-Shen estimator is not sensitive to the value of the Lagrange multiplier in a range of $2,000-50,000$ (Liu 2014). The vorticity (ω), second invariant (Q) and divergence (div) are calculated from the velocity field (see the definitions of these quantities in Section 3). To evaluate the accuracy of the optical flow method, the root mean square (RMS) errors of these quantities are calculated, which are denoted by $RMS(\boldsymbol{u})$, $RMS(\omega)$, $RMS(Q)$, and $RMS(div)$. Table 1 shows the normalized RMS values defined by $RMS(\boldsymbol{u})/max(|\boldsymbol{u}|)$, $RMS(\omega)/max(|\omega|)$, $RMS(Q)/max(|Q|)$, and $RMS(div)/max(|div|)$. The relative RMS errors of the velocity, vorticity, second invariant and divergence are about 17%, 5%, 0.1% and 1%, respectively. The relative errors of the second invariant and divergence are small since their maximum values at the center are large.

To simulate the effect of image noise on optical flow computation, the Gaussian noise is added to the clean cloud image in Fig. 2(a) to produce the noisy cloud image in Fig. 2(b). The mean and standard deviation of the Gaussian noise are zero and 0.015, respectively. The

small local dots are distributed, as shown in Fig. 2(b). The extracted velocity vectors and streamlines from the noisy images are shown in Figs. 3(c) and 4(c), respectively. Although large spiky errors of velocity occur at some isolated locations, the relative RMS error of velocity in the whole image remains about 17%.

We observe that the relative error in the inner region of the images is smaller than the relative error in the outer region. The differences in the errors between the inner and outer regions are caused by differences in the morphologies of these two regions in cloud patterns [see Fig. 2(a)]. There are more discrete cloud features (patches) with large local image intensity gradient $|\nabla I_N|$ in the inner region, while there are less discrete cloud features in the outer region where $|\nabla I_N|$ is smaller. According to an error analysis of optical flow computation, an error is inversely proportional to $|\nabla I_N|$ (Liu and Shen 2008; Liu et al. 2015), and thus the error in the inner region is expected to be smaller than that in the outer region.

Table 1: Relative RMS errors in wind measurement tests using synthetic images

	Velocity	Vorticity	Second Invariant	Divergence
Clean images	0.169	0.046	0.001	0.012
Noisy images	0.171	0.197	0.093	0.057

3. Results

3.1. Mapping

The origin of the image coordinate system (x_1, x_2) is located at the NP is defined in Fig. 5 for image processing. In this study, the image plane is an orthographic projection plane that is parallel to the tangent plane at the NP. Furthermore, there is a one-to-one mapping between the tangent plane at the NP and Saturn's surface. In particular, since the characteristic size of the NPV is much smaller than Saturn's curvature radius (a ratio between

them is about 0.03), the tangent plane at the NP and Saturn's surface is approximately isometric, giving the relative error of the length measure between them is less than 4×10^{-4}. Further, an approximate differential relation between the image coordinates (x_1,x_2) and the oblate spherical coordinates (x,y) in a sufficiently small region is $(dx_1,dx_2)\approx c(dx,dy)$, where the scaling constant, c, is determined by mapping between the oblate coordinates and the imaging coordinates (about 3×10^{-4} pixel m^{-1} as indicated below).

The relationship between the image coordinates and the oblate spherical coordinates is further described below. Following meteorological convections, ϕ and λ denote the latitude and longitude in a spherical coordinate system, respectively (Holton and Hakim 2013). In this work, the planetocentric latitude ϕ_c is used for mapping in all relevant figures, which is related to the planetographic latitude by $\phi_g = arctan\left(\left(R_e / R_p\right)^2 tan\,\phi_c\right)$. The mapping factors in the oblate spherical coordinates are given by

$$r(\phi_g) = \frac{R_e}{\left(1+\left(R_p / R_e\right)^2 tan^2\,\phi_g\right)^{1/2}},\ R(\phi_g) = \frac{r(\phi_g)/cos\,\phi_g}{sin^2\,\phi_g + \left(R_e / R_p\right)^2 cos^2\,\phi_g}, \tag{5}$$

where R_e and R_p are the equatorial and polar radii of the planet, respectively, $r(\phi_g)$ is the distance between a point of the surface and the rotational axis of the planet, and $R(\phi_g)$ is the radius of the curvature of the local meridian. In general, the differential displacements on the surface of Saturn are given by $dx = r(\phi_g)d\lambda$ and $dy = R(\phi_g)d\phi_g$. In this special case where the origin of the surface coordinate system (x,y) is located at the NP, a relevant relation is $dx = dy = R(\phi_g)d\phi_g$. For Saturn, $R_e = 60{,}268\,km$ and $R_p = 54{,}364\,km$ (Seidelmann et al. 2007, Archinal et al. 2009). For the images used in this work, a projection scaling factor is

$\Delta\phi_g = 0.002844\pi / 180$ rad pixel^{-1}. Based on Eq. (5), a converting factor in the image plane is about $3{,}316$ m pixel^{-1} near the NP ($\phi_c = 89^o - 90^o$).

3.2. Temporally averaged maps of wind velocity, vorticity, divergence, and second invariant

Following Sayanagi et al. (2017), after the images were corrected for the net translational motion, they were rotationally transformed to a reference frame that had a planetary rotation rate of 3.138×10^{-4} rad s^{-1}, i.e.,1.5×10^{-4} rad s^{-1} faster than the System III reference frame (Seidelmann et al. 2007; Archinal et al. 2009; Desch and Kaiser 1981). The reference frame transformation was needed in order to reliably make cloud-tracking measurements due to the fast eastward cloud motion in the region. In the transformed reference frame, the cloud motion due to the vortex's wind appears 'frozen' at 88.95 °N latitude. The value of the rotational rate is selected purely for cloud tracking, and it does not affect the final tracking result since an inverse rotational transformation at the same rate will be applied. The resolution and the domain were not changed in the re-mapping process, and resulting maps retain the 1024×1024-pixel polar orthographic projection.

Figure 1 shows the first four of the 14 successive pre-rotated cloud images ($1024\,pix \times 1024\,pix$) near Saturn's NP. Using the optical flow algorithm (Liu 2017), thirteen instantaneous velocity fields are obtained from a time sequence of fourteen pre-rotated images. Figure 6 shows the time-averaged velocity vector field and streamlines of Saturn's NPV obtained from the pre-rotated images, representing the average cloud motion over the whole image sequence. The 1024×1024 velocity vectors are obtained at a spatial resolution of one vector per one pixel. Because map-projected images are rotationally transformed, the extracted velocity field in Fig. 6 has an inner region where the flow rotation is counterclockwise and an outer region where the flow rotation is clockwise. There is a

near-circular boundary at which the velocity is zero between the inner and outer regions, which is a consequence of making the wind measurements in the rotationally transformed coordinate. These artifacts will disappear when an inverse rotational transformation is applied.

Next, the extracted velocity field is reverse-transformed to the original System III reference frame by rotationally transforming the velocity field at a rotational rate of -1.5×10^{-4} rad s^{-1} in the image plane, mapped into the oblate spherical coordinate system. For simplicity of expression, after the above conversion to the System III velocity, the notation $\boldsymbol{u}$ is used to denote the velocity on the tangent plane or Saturn's surface. Since image coverage is incomplete in latitudes lower than 88.5°N, the optical flow computation is carried out in a circular region, which is a common region shared by all the 14 images used in this study. Figure 7 shows the time-averaged velocity vectors and streamlines of the NPV after the inverse rotational transformation is applied. Figure 8(a) shows the time-averaged velocity magnitude field, which illustrates the overall flow structure in the cyclonic inner core of Saturn's NPV, where the velocity magnitude increases with the radial distance from the NP (decreasing latitude) until reaching a maximum speed of ~155 m s^{-1} at 88.95ºN. The estimated uncertainty in extraction of NPV's velocity fields is about 17% (26 m s^{-1}) (see Section 2).

To further understand Saturn's NPV structure, the relative vorticity, divergence and second invariant of the flow field are examined. When the effect of the surface curvature is small, the relative vorticity and divergence can be calculated by using the following approximate relations $\omega=(\nabla\times\boldsymbol{u})\cdot\boldsymbol{e}_3\approx c^{-1}(\partial u_1/\partial x_2-\partial u_2/\partial x_1)$ and $div(\boldsymbol{u})\approx c^{-1}(\partial u_1/\partial x_1+\partial u_2/\partial x_2)$, respectively, where $\boldsymbol{u}=(u_1,u_2)$ is the velocity in the tangent plane at the NP, $\boldsymbol{e}_3$ is the unit vector in the coordinate normal to the plane, and c is a

projection mapping factor (*0.3016* pixel km^{-1}). Note that the divergence $div(\boldsymbol{u})$ is the first invariant of the strain-rate tensor. The second invariant is useful in characterizing the NPV flow structure. The second invariant of the strain-rate tensor can be used to quantify the rotational motion relative to the shearing motion (Hunt et al. 1988). The second invariant Q is defined as $Q = \left(\|\boldsymbol{\Omega}\|^2 - \|\boldsymbol{S}\|^2 \right)/2$, where $\|\boldsymbol{S}\|^2 = tr\left(\boldsymbol{S}\,\boldsymbol{S}^T\right)$ and $\|\boldsymbol{\Omega}\|^2 = tr\left(\boldsymbol{\Omega}\,\boldsymbol{\Omega}^T\right)$, $\boldsymbol{S}$ and $\boldsymbol{\Omega}$ are the symmetric and antisymmetric components of $\nabla\boldsymbol{u}$. The components of $\boldsymbol{S}$ and $\boldsymbol{\Omega}$ are $S_{ij} \approx c^{-1}\left(\partial u_i/\partial x_j + \partial u_j/\partial x_i\right)/2$ and $\Omega_{ij} \approx c^{-1}\left(\partial u_i/\partial x_j - \partial u_j/\partial x_i\right)/2$ $(i,j = 1,2)$. In short, Q represents a balance between the vorticity magnitude and shear strain. When Q is positive, the rotational motion locally prevails over the shearing motion. As the result, a 'vortex' could be defined as a compact region with the positive second invariant Q. We select the method of Hunt et al. (1988) because of its simplicity although this is not the only way to define a vortex.

The physical meaning of $div(\boldsymbol{u})$ can be interpreted as follows. According to the continuity equation for an incompressible flow, the gradient of the velocity component normal to a surface is $\partial u_3/\partial x_3 = -div(\boldsymbol{u})$, where x_3 and u_3 are the coordinate and velocity component normal to the surface and directing outwardly from Saturn's surface. The region with $div(\boldsymbol{u}) > 0$ has an upwelling motion below such that the vertical velocity gradient becomes $\partial u_3/\partial x_3 < 0$. On the other hand, when $div(\boldsymbol{u}) < 0$, the underlying layer has a downwelling motion, which makes the vertical gradient positive ($\partial u_3/\partial x_3 > 0$). As shown in Fig. 8(c), the divergence in the NPV region is non-homogenous, which varies between positive ($div(\boldsymbol{u}) > 0$) and negative ($div(\boldsymbol{u}) < 0$). The region of the positive divergence to the left of the center of the NPV shown in Fig. 8(c) indicates a localized region of upwelling.

Figures 8(b), 8(c) and 8(d) show maps of the temporally averaged relative vorticity, divergence and second invariant. As shown in Fig. 8(b), the relative vorticity is generally positive, indicating cyclonic rotation, and its magnitude increases toward the NP. There are near-circular band patterns with distinct fine vorticity patches in the NPV, which could be generated by shear instabilities. Furthermore, Figure 8(d) indicates that regions with the positive second invariant are concentrated near the NP, highlighting strong rotational motion.

From a perspective of image processing, as shown in Fig. 5, it is convenient to use a polar coordinate system (λ, r) in the orthographically projected image plane, where λ is the polar angle, r is the radial coordinate, and $\boldsymbol{s}$ is the unit tangent vector along a circular arc. This polar coordinate represents the orthographically-projected version of the oblate spherical coordinate, where λ is the longitude and r is the distance between a point of the surface and Saturn's rotational axis. Accordingly, the velocity $\boldsymbol{u}$ can be decomposed into the circumferential and radial components u_c and u_r, where u_c is positive for counter-clockwise flow and u_r is positive for radially outward flow. Thus, u_c is the zonal velocity, and $-u_r$ is interpreted as the meridional velocity in the sign convention of geophysical fluid mechanics. The dominant velocity component is u_c as shown in Fig. 7. Using this notation, averaged profiles over a polar angle range $\lambda \in [0, 2\pi]$ can be calculated. Figure 9 shows the profiles of $\langle u_c \rangle_\lambda$ (the zonal velocity) and $-\langle u_r \rangle_\lambda$ (the meridional velocity) as functions of the planetocentric latitude, where $\langle \bullet \rangle_\lambda$ denotes a averaged quantity in $\lambda \in [0, 2\pi]$ along a circular arc with the unit vector $\boldsymbol{s}$. The profile of the zonal velocity $\langle u_c \rangle_\lambda$ is consistent with that extracted by using the correlation image velocimetry (CIV) with interrogation windows of 30×30 pixels (about $60\,\mathrm{km} \times 60\,\mathrm{km}$ in the physical space) for computation of cross-correlation (Sayanagi et al. 2017). The peak velocity of 150 m s^{-1} given by CIV is about 17%

slower than that calculated in the current work using the optical flow method. Antunano et al. (2018) also used a CIV to report velocity profiles slightly slower than those found by Sayanagi et al. (2017) with interrogation windows of 80×80 pixels (about $466\,km \times 466\,km$ in the physical space). The difference between Sayanagi et al. (2017) and Antunano et al. (2018) is consistent with the use of larger interrogation windows tending to underestimate the velocity magnitude. The location of the peak zonal wind is at $\phi_c = 88.95^o$ latitude, which is consistent with the value given by Sayanagi et al. (2017) and Antuñano et al. (2018). The variation bounds indicated in Fig. 9 mainly represent the temporal-spatial changes of the velocity structures in ensemble averaging and averaging over a polar angle range $\lambda \in [0, 2\pi]$. In addition, they include the uncertainties in the optical flow computation (see Table 1).

Some vortex solutions of the Navier-Stokes equations are available for comparison with the NPV flow structure (e.g., Wu et al. 2006), to describe the structures of large-scale vortices in geophysical flows, as done previously by Wood and White (2011) and Greenleaf (2011). Here, a Burgers vortex is selected for comparison with the NPV's measured velocity profile due to its structural simplicity, particularly in the inner region. The circumferential (tangential) velocity of a Burgers vortex is given by $u_c = r^{-1}\left(1 - exp\left(-r^2 / r_0^2\right)\right)$, where r is the radial coordinate and r_0 is a constant controlling the size of the vortex. An intriguing question is whether the NPV can be approximately described as a Burgers vortex. To compare the NPV with a Burgers vortex model, the zonal velocity $\langle u_c \rangle_\lambda$ is normalized by $max\left(\langle u_c \rangle_\lambda\right)$ and the radial coordinate r is normalized by the radial distance at which $max\left(\langle u_c \rangle_\lambda\right)$ is reached. The normalized velocity profiles are collapsed into a single curve, as shown in Fig. 10. The normalized zonal velocity profiles obtained by both the optical flow method and CIV compare well with the inner velocity distribution of a Burgers vortex model.

A Burgers vortex also has a radial velocity proportional to r and an axial velocity proportional to the vertical coordinate z. Although the average radial velocity, $\langle u_r \rangle_\lambda$, of the NPV is small overall, close inspection indicates that the value of $\langle u_r \rangle_\lambda$ is positive in the region near the NP ($\phi_c = [89.2^o, 90^o]$), which could be associated with outwardly-spiraling streamlines revealed in Fig. 7(b). This problem will be further discussed later.

Figure 11 shows the profiles of $\langle \omega \rangle_\lambda$, $\langle div(\boldsymbol{u}) \rangle_\lambda$ and $\langle Q \rangle_\lambda$ as a function of the planetocentric latitude. The profile of $\langle \omega \rangle_\lambda$ in Fig. 11(a) confirms that the relative vorticity is positive and high near the NP, indicating cyclonic rotation. Interestingly, the profile of $\langle div(\boldsymbol{u}) \rangle_\lambda$ is relatively small and uniform across the latitude, as shown in Fig. 11(a). The small region with low $\langle div(\boldsymbol{u}) \rangle_\lambda$ implies that the local positive and negative components of the divergence tend to cancel out each other in averaging along longitude. This observation will be confirmed by the probability density function (pdf) of the divergence in Section 3.3. Nevertheless, in the region near the NP, the averaged divergence has a positive value, indicating weak upwelling motion that corresponds to outwardly spiraling streamlines illustrated in Fig. 7(b). The variation bounds in Fig. 11 mainly represent the temporal-spatial changes of the corresponding quantities, which also include contributions by the error in the optical flow computation. See the error analysis in Section 2.2 for details.

3.3. Statistics

The averaged fields of the vorticity, divergence and second invariant in Fig. 8 exhibit some fine structures. The quasi-random small-scale structures superposed on the well-defined time-averaged NPV are evident particularly in instantaneous fields (see Figs. 17-19). The statistics of these quantities may provide useful insights into the structure of the NPV. To remove the random image noise and distill the flow structures, the velocity fields are

filtered using a Gaussian filter that smooths features smaller than 50 pixels, and then a sample body of data is reconstructed in the measurement domain of 1024×1024 pixels from the 13 instantaneous fields. The probability density functions (pdfs) of the vorticity, divergence and second invariant are computed based on sample bodies.

Figure 12 shows the pdfs of the vorticity, divergence and second invariant in comparison with the Gaussian distribution with the same mean value and standard deviation. The mean value, standard deviation (std), skewness and kurtosis of the measured distributions are listed in Table 2. As shown in Fig. 12(a), the pdf of the vorticity is non-Gaussian, which has the mean value of $3.2 \times 10^{-4}\ s^{-1}$ and the std of $1.5 \times 10^{-4}\ s^{-1}$. The pdf has a skewness of 0.53, and the longer tail on the positive side exhibits spatial intermittency of high vorticity structures. The intermittent features are evidenced by highly localized spots in the instantaneous vorticity fields shown in Fig. 16. Note that intermittency of high vorticity structures is an intrinsic property of turbulence (Frisch 1995). The kurtosis (flatness) of the pdf is 3.2, which is close to that of a Gaussian distribution.

As shown in Fig. 12(b), the pdf of the divergence is near-symmetrical since the skewness is -0.1. The mean value of $1.5 \times 10^{-6}\ s^{-1}$ is much smaller than the std of $5.8 \times 10^{-5}\ s^{-1}$. The pdf of the divergence indicates that the structures with the positive and negative divergence (corresponding to upwelling and downwelling) have almost the same probability of occurrence. The pdf of the divergence has a kurtosis of 3.7, which is slightly peaked. In Fig. 12(c), the pdf of the second invariant has a mean value of $1.6 \times 10^{-8}\ s^{-1}$, and a std of $2.3 \times 10^{-8}\ s^{-1}$, which is moderately skewed towards the positive side with a skewness of 1.1. This means that the rotational motion in the NPV prevails over the shearing motion. The longer tail on the positive side indicates the spatial intermittency of strong rotational

motions, which is consistent with that of the vorticity. The pdf of the second invariant with a kurtosis of *5.3* is much more peaked than a Gaussian distribution.

Table 2. Statistical quantities on the pdf of the vorticity, divergence, and second invariant.

	Vorticity (s^{-1})	Divergence (s^{-1})	Second Invariant (s^{-2})
Mean value	3.2×10^{-4}	1.5×10^{-6}	1.6×10^{-8}
Standard deviation	1.1×10^{-4}	5.8×10^{-5}	2.3×10^{-8}
Skewness	0.53	-0.1	1.1
Kurtosis	3.2	3.7	5.3

3.4. Instantaneous fields

The temporally-averaged wind field of the NPV has the highly concentrated positive vorticity and secondary invariant near the center and spatially varying divergence. To further examine NPV's dynamics, the instantaneous flow fields are examined. Figures 13, 14 and 15 show the first three instantaneous fields of the velocity vectors, streamlines and velocity magnitude, respectively, which are extracted from the first four cloud images (see Fig. 1); the time intervals between the sequential image pairs are 21.9, 28.4, and 20.5 min, respectively. The overall patterns of these instantaneous fields are similar to the time-averaged flows shown in Fig. 8.

Nevertheless, as shown in Figs. 16-18, clusters of distinct isolated small structures occur in the vorticity, divergence, and second invariant fields, particularly in the NPV's inner region (89.2°N-90°N). The first question that arises in regards to these small structures is whether they are artifacts generated by the error associated with the image intensity gradient magnitude patterns (Liu and Shen 2008). To examine this problem, the intensity gradient magnitudes are calculated for the mapped images, and the intensity gradient for the first 4 maps, corresponding to those shown in Fig 1, are presented in Fig. 19. If these patterns are similar to the structures in Figs. 16-18, the results extracted by using the optical flow method could be negatively impacted by a fixed-pattern error that is associated with a spatially

distribution of image intensity gradient magnitude (Liu and Shen 2008). The correlation coefficients between the images in Fig. 19 and those in Figs. 16-18 are evaluated. The correlation coefficient between the fixed-pattern error and the vorticity field is 0.025-0.063. The correlation coefficients for the divergence and second invariant fields are 0.113-0.209 and 0.054-0.089, respectively. The small correlation coefficients indicate that the small structures in Figs. 16-18 are not associated with the fixed-pattern error in the optical flow computation.

Another question that arises is whether these isolated small structures are physically real. To address this question, additional evidence is required. First, the instantaneous divergence fields in Fig. 17 are examined, indicating that there are distinct positive divergence spots in the generally negative divergence region. This result is consistent with the observation of large particle condensate cloud patterns by Baines et al. (2018) inferring the existence of convective upwelling. Next, as discussed in Section 3.3, the distinct vortical structures with the positive vorticity and second invariant in Figs. 16 and 18 could be generated and intensified by local convective instability in regions with $div(\boldsymbol{u}) > 0$.

The time-averaged positive divergence corresponds to the negative radial or meridional velocity ($-\langle u_r \rangle_\lambda$) near the NP, which is manifested by outwardly spiraling streamlines and could be caused by upwelling associated with convective instability. An intriguing question is how far this outwardly spiraling motion could extend. It is noticed that the available data outside this circular region in some regions of the image could be used to infer the flow behavior in the outer ring of $\phi_c = 85.6^o - 88.95^o$. Figure 20 shows the meridional velocity profile ($-\langle u_r \rangle_\lambda$) averaged over $\lambda \in [0, 2\pi]$ based on the first three instantaneous fields. Indeed, streamlines moderately spiral outward near the NP since $\langle u_r \rangle_\lambda$ is positive in $\phi_c = 89.27^o - 90^o$, as shown in Fig. 21. In contrast, streamlines spiral inwardly in the outer

ring since $\langle u_r \rangle_\lambda$ is negative at $\phi_c < 89.27^o$. The zero-crossing point is at $\phi_c = 89.27^o$, delineating a circle in which the outwardly-spiraling motion is limited. Phenomenologically, this circle is considered as a stable limit cycle to which neighboring streamlines tend to converge (Hurewicz 2002).

3.5. Discussion

From a topological perspective, as shown in Fig. 14, the center of the NPV is considered as a cyclonic outwardly-spiraling node. A question is whether this node is physically possible. It is conjectured that this node is associated with upwelling driven by the vertical temperature gradient generated by a localized heat source underneath. To elucidate the generation of this outwardly-spiraling node, a localized quasi-one-dimensional (quasi-1D) analysis is given here. Note that this is not a quasi-geostrophic analysis.

For simplicity of a quasi-1D fluid-mechanic analysis, it is natural to select the vertical coordinate z pointing into a fluid layer below the cloud top at the NP, and denote w as the corresponding vertical velocity. Although these notations are opposite to those in conventional meteorological analysis where z and w point upward, the relevant quantities $\partial w / \partial z$ and $div(\boldsymbol{u})$ remain invariant. In addition, the main result derived in this analysis, Eq. (10), remains formally valid even though the sign of the vorticity is defined differently. As illustrated in Fig. 22, we consider a fluid element travelling vertically over a displacement δz. The fluid motion along the z-axis through the center is locally dominated by the buoyancy force. The vertical momentum equation near a reference location z_0 of a differential material element with a vertical length δz can be approximately written as (McWilliams 2006)

$$Dw / Dt \approx -N^2(z_0)\delta z, \tag{6}$$

where $N^2 = (g/T)(\partial T/\partial z + g/c_p)$ is the square of the buoyancy frequency (N). This frequency depends on the vertical temperature gradient $\partial T/\partial z$, the local temperature T, the gravity constant g, and the specific heat c_p. We can use a first-order Taylor-series approximation near a reference location z_0 for the vertical velocity gradient, i.e., $\partial w/\partial z \approx \delta w/\delta z = [w(z) - w(z_0)]/\delta z$. Since the vertical derivative of w is $\partial w/\partial z = -div(\boldsymbol{u})$ for an incompressible flow, the vertical velocity is approximately expressed as $w(z) \approx w(z_0) + \delta z\, \partial w/\partial z = w(z_0) - \delta z\, div(\boldsymbol{u})$. Here we call $div(\boldsymbol{u})$ the sectional divergence since it is related to the two cloud-top velocity components. Since the fixed vertical length δz can be moved into the operator D/Dt in Eq. (6), a transport equation for the sectional divergence is given as

$$D(div(\boldsymbol{u}))/Dt \approx N^2, \tag{7}$$

where N^2 acts as a driving term to generate $div(\boldsymbol{u})$.

When a fluid element moving vertically is followed upwards from an initial deeper position in a fluid layer to the cloud top, the material derivative of the fluid particle is replaced by the ordinary time derivative, i.e., $D/Dt = d/dt$, and a formal solution of Eq. (7), in the Lagrangian framework, is

$$div(\boldsymbol{u}) \approx \int_0^t N^2[z(t')]dt', \tag{8}$$

where $z(t)$ denotes the time-dependent vertical position of the moving fluid element. According to Eq. (8), the cloud-top divergence as a time integral of N^2 is positive, and it is enhanced due to a convection history as the fluid element travels from the inside of the layer to the cloud top. The above analysis reveals a direct relationship between the source node at the NP and the convective instability.

In a quasi-1D approximation at the NP, the vorticity is $\boldsymbol{\omega}=(0,0,\omega_z)$ and the rotational rate of the planet is $\boldsymbol{\Omega}=(0,0,\Omega_z)$, where ω_z and Ω_z are the components along the z-axis. Thus, for an incompressible flow, the vorticity equation is written as (Pedlosky 1979)

$$D\omega_{a,z}/Dt=-div(\boldsymbol{u})\omega_{a,z}+S_z, \tag{9}$$

where $\omega_{a,z}=\omega_z+2\Omega_z$ is the *z*-component of the absolute vorticity and $S_z=(\nabla\rho\times\nabla p)_z/\rho^2$ is the *z*-component of the baroclinic vector. In the right-hand side (RHS) of Eq. (9), the first term represents the vortex stretching by the vertical velocity gradient $\partial w/\partial z$, and the second term is the baroclinic vector as a source term. In following a fluid element, a formal solution of Eq. (9) is

$$\begin{aligned}\frac{\omega_{a,z}}{\omega_{a,z0}}=&exp\left(-\int_0^t div(\boldsymbol{u})dt'\right)\\&\times\left\{1+\int_0^t S_z\,exp\left(\int_0^{t'}div(\boldsymbol{u})dt''\right)dt'\right\},\end{aligned} \tag{10}$$

where $\omega_{a,z0}$ is an initial value of $\omega_{a,z}$ at a reference location z_0 at t = 0. Eq. (10) gives a connection between the sectional divergence and the vorticity. The first exponential factor represents the direct effect of the sectional divergence on the generation of the vorticity. For $div(\boldsymbol{u})>0$ in a source velocity field, this factor contributes a decay of the vorticity as a fluid element moves up. The second factor represents the vorticity generation by interaction between the sectional divergence and baroclinic vector. According to Eq. (8), for $N_s^2>0$, the sectional divergence is $div(\boldsymbol{u})>0$, which leads to a source node at the cloud top. As a result, according to Eq. (10), positive vorticity is generated as a fluid particle moves up, which causes the cyclonic rotational motion. This provides an explanation for the observed outwardly-spiraling cyclonic node at the NP.

Outside the outwardly-spiraling flow region ($\phi_c < 89.27^o$), the meridional velocity could be positive towards the pole. In the outer region where the convective instability is not considered, the flow is mainly driven by the pressure gradient and the Coriolis force, and in the geostrophic approximation the cloud-top velocity is given by $\boldsymbol{u} = (\boldsymbol{k} \times \nabla p) / f\rho_s$, where $\boldsymbol{k}$ is the unit vector normal to the surface and ρ_s is the reference density in the absence of motion (Pedlosky 1979). Therefore, streamlines in the outer region are near-circular, which is confirmed by the optical flow measurements. In the cloud-top velocity field, the boundary between the outwardly-spiraling flow region and the outer region is considered as a stable limit cycle, which is defined as a closed loop to which neighboring streamlines converge (Hurewicz 2002). Since the flow is 3D, as illustrated in Fig. 22, we conjecture that this limit cycle is an orthographical projection of a cylindrical shear layer on which the flow cyclonically spirals downward. This shear layer is located at about $\phi_c = 89.27^o$, which corresponds to the zero-crossing point in Fig. 20. Furthermore, we hypothesize that a vertical circulation flow is trapped in a cylindrical domain as illustrated in Fig. 22. The Navier-Stokes equations could permit a solution in convection-driven rotational flow that is similar to the Sullivan two-cell vortex (Sullivan 1959). The conjectured flow also matches an experimentally modeled 3D vortex intensified by thermal convection (Makhmalbaf et al. 2017).

4. Conclusions

The time-averaged velocity field shows a well-defined counter-clockwise (cyclonic) vortex at the NP. The velocity variation in the measurement domain over the observation timespan is less than 10%. The mean zonal (circumferential) velocity increases with the decreasing latitude or the increasing radial distance from the NP, and the location of the peak value is at

$\phi_c = 88.95^o$. The extracted zonal velocity profile compares well to a Burgers vortex model for the inner core of the NPV. The mean meridional velocity is overall small in magnitude, but it is negative in the region near the NP, which corresponds to observed outwardly spiraling streamlines. The relative vorticity and second invariant are concentrated near the NP, indicating strong rotational motion of the fluid. This spiraling source node at the NP could be generated by thermal convective instability according to a quasi-1D fluid-mechanic analysis. In the instantaneous fields of the vorticity, divergence and second invariant, distinct isolated small structures are observed. The instantaneous divergence fields exhibit local positive (upwelling) and negative (downwelling) patches manifesting as local 3D structures. In addition, the distinct vortical structures with the positive vorticity and second invariant are observed, which could be generated and intensified by local convective instability in regions with the positive divergence.

Acknowledgements:

KMS was supported by NASA Cassini Data Analysis Program Grant NNX15AD33G. SRB was supported by NASA NESSF Grant NNX16AP44H.

The data used to generate the figures in this paper are available in "Saturn_NPV_Velocity_Data" at Harvard Dataverse. The link is https://dataverse.harvard.edu/dataset.xhtml?persistentId=doi%3A10.7910%2FDVN%2FOPLQCL

References:

Archinal, B. A.; A'Hearn, M. F., Bowell, E.; Conrad, A.; Consolmagno, G. J., Courtin, R.; Fukushima, T.; Hestroffer, D., Hilton, J. L.; Krasinsky, G. A.; Neumann, G.; Oberst, J.; Seidelmann, P. K.; Stooke, P.; Tholen, D. J., Thomas, P. C. & Williams, I. P. (2009) Report of the IAU Working Group on Cartographic Coordinates and Rotational Elements. Celestial Mechanics and Dynamical Astronomy 109(2), 101-135. doi 10.1007/s10569-010-9320-4.

Antuñano, A., del Río-Gaztelurrutia, T., Sánchez-Lavega, A., and Hueso, R. (2015). Dynamics of Saturn's polar regions. J. Geophys. Res. Planets 120, 155–176. doi 10.1002/2014JE004709.

Antuñano, A., del Río-Gaztelurrutia, T., Sánchez-Lavega, A., and Rodriguez-Aseguinolaza, J. (2018). Cloud morphology and dynamics in Saturn's northern polar region. Icarus 299, 117-132. doi 10.1016/j.icarus.2017.07.017.

Asay-Davies, X., Marcus, P., Wong, W., and de Pater, L. (2009). Jupiter's shrinking Great Red Spot and steady Oval BA: velocity measurements with the 'Advection Corrected Correlation Image Velocimetry' automated cloud-tracking method. Icarus, 203, 164. doi 10.1016/j.icarus.2009.05.001.

Baines, K., Momary, T., Temma, T., Buratti, B., Roos-Serote, M., Showman, A., Brown, R., Clark, R., Nicholson, P., Atreya, S., Graham, J., and Marquez, E. (2007). The structure of Saturn's poles determined by Cassini/VIMS: Constraints on winds and horizontal and vertical cloud distributions. American Astronomical Society, DPS meeting #39, id.9.02; Bulletin of the American Astronomical Society, Vol. 39, p.423.

Baines, K., Momary, T., Fletcher, L., Showman, A., Roos-Serote, M., Brown, R., Buratti, B., Clark, R., and Nicholson, P. (2009). Saturn's north polar cyclone and hexagon at depth

revealed by Cassini/VIMS. Planetary and Space Science, 57, 1671-1681. doi 10.1016/j.pss.2009.06.026.

Baines, K. H., Sromovsky, L. A., Fry, P. M., Momary, T. W., Brown, R. H., Buratti, B. J., et al. (2018). The eye of Saturn's north polar vortex: Unexpected cloud structures observed at high spatial resolution by Cassini/VIMS. Geophysical Research Letters, 45, 5867–5875. doi 10.1029/2018GL078168.

Cheng, A. F., Simon-Miller, A. A., Weaver, H. A., Baines, K. H., Orton, G. S., Yanamandra-Fisher, P. A., Mousis, O., Pantin, E., Vanzi, L., Fletcher, L. N., Spencer, J. R., Stern, S. A., Clarke, J. T., Mutchler, M. J., Noll, K. S., (2008). Changing characteristics of Jupiter's Little Red SPOT. Astronomical Journal, 135, 2446-2452. doi 10.1088/0004-6256/135/6/2446.

Choi, D., Banfield, D., Gierasch, P., and Showman, A. (2007). Velocity and vorticity measurements of Jupiter's Great Red Spot using automated cloud feature tracking. Icarus, 188, 35. doi 10.1016/j.icarus.2006.10.037.

Choi, D., Showman, A., and Brown, R. (2009). Cloud features and zonal wind measurements of Saturn's atmosphere as observed by Cassini/VIMS. J. Geophys. Res., 114, E04007. doi 10.1029/2008JE003254.

Choi, D. S., Showman, A. P., Vasavada, A. R., (2010). The evolving flow of Jupiter's White Ovals and adjacent cyclones. Icarus 207, 359-372. doi 10.1016/j.icarus.2009.10.013.

Desch, M. D.; Kaiser, M. L. (1981) Voyager measurement of the rotation period of Saturn's magnetic field. Geophysical Research Letters, 8(3), 253-256.

Dowling, T.E. and Ingersoll, A.P. (1988) Potential vorticity and layer thickness variation in the flow around Jupiter's Great Red Spot and white Oval BC. J. of the Atmospheric Sciences, 45(8), 1380-1396. doi 10.1175/1520-0469(1988)045<1380:PVALTV>2.0.CO;2.

Dowling, T., Fisher, A., Gierasch, P., Harrington, J., LeBeau, R., and Santori, C. (1998) The explicit planetary isentropic-coordinate (EPIC) atmospheric model. Icarus 132, 221-238. doi 10.1006/icar.1998.5917.

Dyudina, U., Ingersoll, A., Ewald, S., Vasavada, A., West, R., Baines, K., Momary, T., Del Genio, A., Barbara, J., Porco, C., Achterberg, R., Flasar, F., Simon-Miller, A., Fletcher, L. (2009). Saturn's south polar vortex compared to other large vortices in the solar system. Icarus 202, 240–248. doi 10.1016/j.icarus.2009.02.014.

Fletcher, L., Irwin, P., Orton, Tenby, N., Achterberg, R., Bjoraker, G., Read, P., Simon-Miller, A., Howett, C., de Kok, R., Bolwes, N., Calcutt, S., Hesman, B., and Flasar, F. (2008). Temperature and composition of Saturn's polar hot spots and hexagon. Science 319(5859), 70–82. doi 10.1126/science.1149514.

Frisch, U. (1995). Intermittency. In *Turbulence: The Legacy of A. N. Kolmogorov* (pp. 120-194). Cambridge: Cambridge University Press. doi:10.1017/CBO9781139170666.009

Garcia-Melendo, E., S Lanchez-Lavega, A., (2001). A Study of the Stability of Jovian Zonal Winds from HST Images: 1995-2000. Icarus 152, 316-330. doi 10.1006/icar.2001.6646.

Godfrey, D. (1988). A hexagonal feature around Saturn's north pole. Icarus, 76, 335–356. doi.org/10.1016/0019-1035(88)90075-9.

Greenleaf, L. R. (2011). Model selection and inference for atmospheric vortices, Proceedings of the 35th Conference on Radar Meteorology, American Meteorological Society, Pittsburg, PA, 26-30 September 2011.

Heitz, D., Memin, E., and Schnorr, C. (2010). Variational fluid flow measurements from image sequences: synopsis and perspectives. Experiments in Fluids, 48, 369-393. doi 10.1007/s00348-009-0778-3.

Mitchell, J.L., Beebe, R.F., Ingersoll, A.P., and Carneau, G.W. (1981) Flow fields with Jupiter's Great Red Spot and white oval BC. J. of Geophysical Research, 86(A10), 8751-8757. doi.org/10.1029/JA086iA10p08751.

Hooke, R., (1665). A spot on one of the belts of Jupiter. Philosophical Transactions of the Royal Society, 1(1), 3. doi.org/10.1098/rstl.1665.0005.

Holton, J. and Hakim, G. (2013). *Introduction to dynamic meteorology* (5th edition). Elsevier, New York. doi 10.1016/B978-0-12-384866-6.00039-8.

Horn, B. and Schunck, B. (1981). Determining optical flow. Artificial Intelligence, 17(1-3), 185-204. doi 10.1016/0004-3702(81)90024-2.

Hueso, R., Legarreta, J., Garcia-Melendo, E., Sanchez-Lavega, A., Perez-Hoyos, S., (2009). The jovian anticyclone BA. II. Circulation and interaction with the zonal jets. Icarus 203(2), 499-515. doi 10.1016/j.icarus.2009.05.004.

Hunt, J., Wray, A., and Moin, P. (1988). Eddies, stream, and convergence zones in turbulent flows. Center for Turbulence Research Report CTR-S88, p. 193.

Hurewicz, W. (2002). *Lectures on ordinary differential equations*, Dover, New York.

Kouyama, T., Imamura, T., Nakamura, M., Satoh, T., and Futaana, Y. (2012). Horizontal structure of planetary-scale waves at the cloud top of Venus deduced from Galileo SSI images with an improved cloud-tracking technique. Planetary and Space Science 60, p.207-216. doi.org/10.1016/j.pss.2011.08.008.

Kouyama, T., Imamura, T., Nakamura, M., Satoh, T., and Futaana, Y. (2013). Long-term variation in the cloud-tracked zonal velocities at the cloud top of Venus deduced from Venus Express VMC images. Journal of Geophysical Research: Planets 118, pp. 37-46. doi 10.1029/2011JE004013.

Limaye, S. S., (1986). Jupiter - New estimates of the mean zonal flow at the cloud level. Icarus 65, 335-352. doi 10.1016/0019-1035(86)90142-9.

Lindal, G. F., Sweetnam, D. N. and Eshleman, V. R. (1885). The atmosphere of Saturn - an analysis of the Voyager radio occultation measurements. Astronomical Journal 90, 1136-1146. doi 10.1086/113820.

Liu, T. and Shen, L. (2008). Fluid flow and optical flow. J. Fluid Mech. 614, 253. doi. 10.1017/S0022112008003273.

Liu, T. Wang, B. and Choi. D. (2012). Flow structures of Jupiter's Great Red Spot extracted by using optical flow method. Physics of Fluids, 24, 096601-13. doi 10.1063/1.4752227.

Liu, T. (2014). Jupiter and Saturn's unique flow structures extracted from cloud images by using optical flow method. 52nd AIAA Aerospace Sciences Meeting, National Harbor, Maryland, 13-17 January.

Liu, T., Merat, A.,Makhmalbaf, M., Fajardo, C. and Merati, P. (2015) Comparison between optical flow and cross-correlation methods for extraction of velocity fields from particle images, Experiments in Fluids, 56, 166-189. doi 10.1007/s00348-015-2036-1.

Liu, T. (2017). OpenOpticalFlow: An open source program for extraction of velocity fields from flow visualization images. Journal of Open Research Software, 5:29. doi.org/10.5334/jors.168.

Makhmalbaf, M. H., Liu, T. and Merati, P. (2017) A vortex flow intensified by thermal convection, Physics of Fluids, 29: 016603. doi.org/10.1063/1.4974754.

McWilliams, J. C. (2006) *Fundamentals of geophysical fluid dynamics*. Cambridge University Press, Cambridge, pp. 78-80. doi 10.2277/052185637X.

Pedlosky, P. (1979) Geophysical fluid mechanics, Springer, Berlin. doi 10.1007/978-1-4612-4650-3.

Sada, F., Beebe, R.F. and Conrath, B.J. (1996) Comparison of the surface and dynamics of Jupiter's Great Red Spot between the Voyager 1 and 2 encounters. ICARUS, 119, 311-335. doi 10.1006/icar.1996.0022.

Sánchez-Lavega, A., Rojas, J.F., and Sada, P.V. (2000). Saturn's zonal winds at cloud level. Icarus 147, 405–420. doi 10.1006/icar.2000.6449.

Sánchez-Lavega, A., Hueso, R., Pérez-Hoyos, S., and Rojas, J. (2006). A strong vortex in Saturn's south pole. Icarus 184, 524–531. doi 10.1016/j.icarus.2006.05.020.

Sayanagi, K. M., Dyudina, U. A., Ewald, S. P., Muro, G. D., Ingersoll, A. P., West, R.A., Porco, C. C., (2011). Dynamics of Saturn's Great Storm of 2010-2011 from Cassini ISS and RPWS. Icarus, 223, p. 460-478. doi 10.1016/j.icarus.2012.12.013.

Sayanagi, K., Dyudina, U., Ewald, S., and Ingersoll, A. (2017). Cassini ISS observation of Saturn's north polar vortex and comparison to the south polar vortex. Icarus 285, 68-82. doi 10.1016/j.icarus.2016.12.011.

Sayanagi, K. M., Baines, K. H., Dyudina, U. A., Fletcher, L. N., Sanchez-Lavega, A., and West, R. A., (2019) Saturn's polar atmosphere. In: K. H. Baines, F. M. Flasar, N. Krupp, T. Stallard, eds. *Saturn in the 21st Century*. Cambridge: Cambridge University Press. doi 10.1017/9781316227220.012.

Seidelmann, P. Kenneth; Archinal, B. A.; A'Hearn, M. F.; Cruikshank, D. P.; Hilton, J. L.; Keller, H. U.; Oberst, R. J.; Simon, J. L.; Stooke, P.; Tholen, D. J.; Thomas, P. C. (2007) Working Group on Cartographic Coordinates and Rotational Elements. IAU Transactions, Vol. 26A, Reports on Astronomy 2002-2005. Edited by O. Engvold. Cambridge: Cambridge University Press, pp.181-181. doi 10.1017/S1743921306004492.

Simon-Miller, A.A., Gierasch, P.J., Beebe, R.F., Conrath, B., Flasar, F.M., Achterberg, R. and the Cassini CIR Team (2002) New observational results concerning Jupiter's Great Red Spot. Icarus, 158, 249-266. doi 10.1006/icar.2002.6867.

Simon-Miller, A. A., Conrath, B. J., Gierasch, P. J., Orton, G. S., Achterberg, R. K., Flasar, F. M., Fisher, B. M., (2006). Jupiter's atmospheric temperatures: From Voyager IRIS to Cassini CIRS. Icarus 180, 98-112. doi 10.1016/j.icarus.2005.07.019.

Simon-Miller, A. A., Poston, B. W., Orton, G. S., Fisher, B., (2007). Wind variations in Jupiter's equatorial atmosphere: A QQO counterpart? Icarus 186, 192-203. doi 10.1016/j.icarus.2006.08.009.

Simon-Miller, A. A., Gierasch, P. J., (2010). On the long-term variability of Jupiter's winds and brightness as observed from Hubble. Icarus 210, 258-269. doi 10.1016/j.icarus.2010.06.020/

Studwell, A., Liming, L., Jiang, X., Baines, K. H., Fry, P. M., Momary, T.W., and Dyudina, U. A. (2018). Saturn's global zonal winds explored by Cassini/VIMS 5-micron images. Geophys. Res. Lett. 45(14), 6823-6831. doi 10.1029/2018GL078139.

Sullivan, R.D., (1959). A two-cell vortex solution of the Navier-Stokes equation. Journal of the Aerospace Sciences, 26(11), 767-768. doi 10.2514/8.8303.

Sussman, M. G., Chanover, N. J., Simon-Miller, A. A., Vasavada, A. R., Beebe, R. F., (2010). Analysis of Jupiter's Oval BA: A streamlined approach. Icarus 210, 202-210. doi 10.1016/j.icarus.2010.06.044.

Vasavada, A. and 12 authors (1998) Galileo imaging of Jupiter's atmosphere: The Great Red Spot, equatorial region, and white ovals. ICARUS, 135, 265-275. doi 10.1006/icar.1998.5984.

Wang, B., Cai, Z., Shen, L., and Liu, T. (2015). An analysis of physics-based optical flow method. Journal of Computational and Applied Mathematics, 276, 62-80. doi 10.1016/j.cam.2014.08.020.

Wood, V. T., and White, L. W., (2011) A New Parametric model of vortex tangential-wind profiles: development, testing, and verification, Journal of the Atmospheric Sciences, 68, 990-1006. doi 10.1175/2011JAS3588.1.

Wu, J. Z., Ma, H. Y. and Zhou, M. D., (2006). Vorticity and vortex dynamics, Springer, Berlin. doi 10.1007/978-3-540-29028-5.

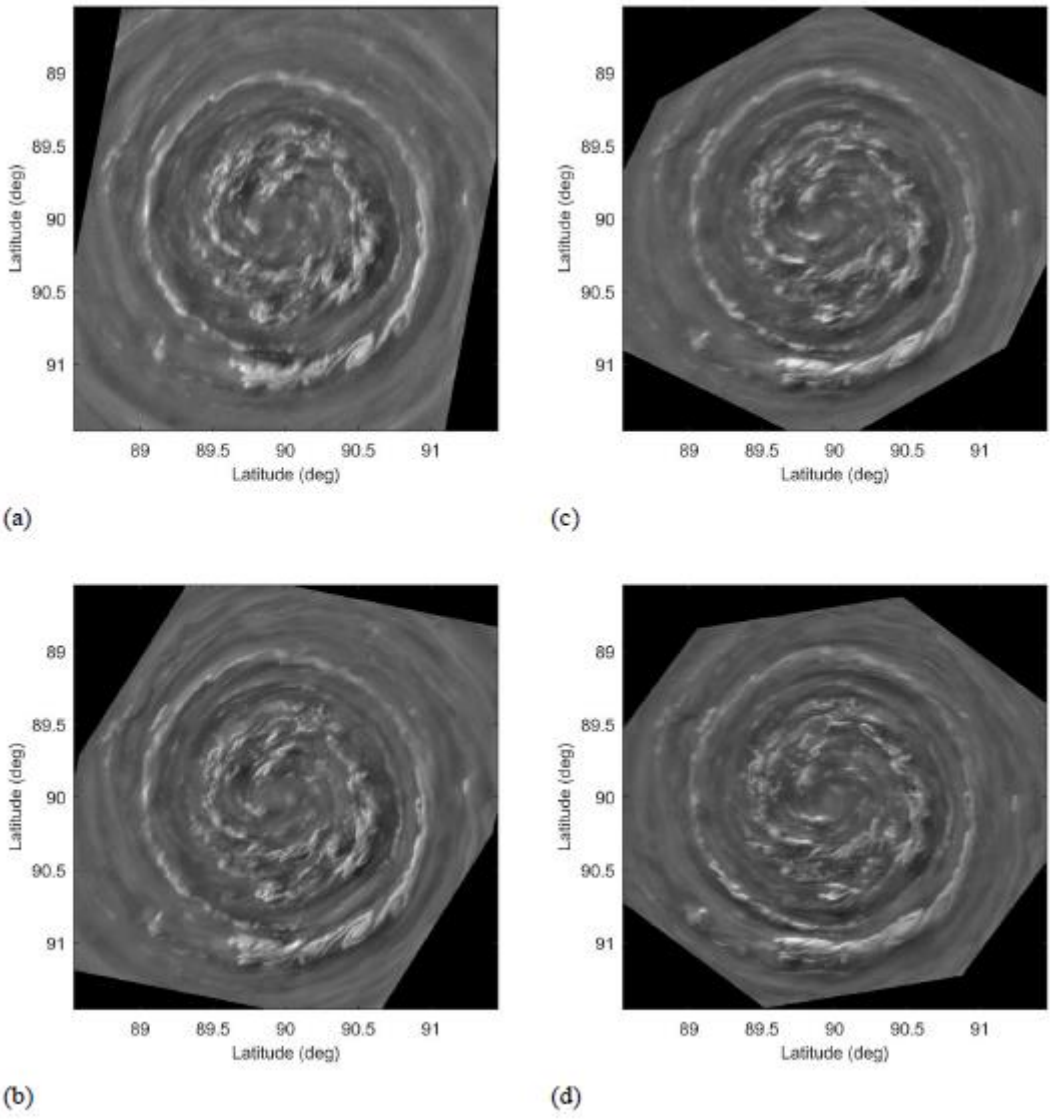

Figure 1. The first four cloud images of Saturn's north pole (NP) region, where the time intervals between the sequential image pairs are 21.9, 28.4, and 20.5 min, respectively.

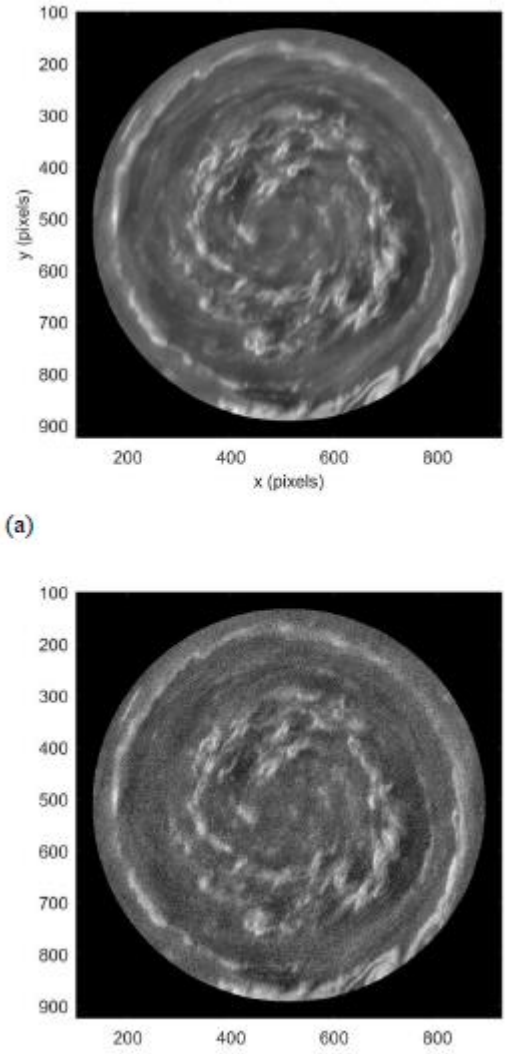

Figure 2. Cloud images of the NPV for simulations: (a) clean image, and (b) noisy image.

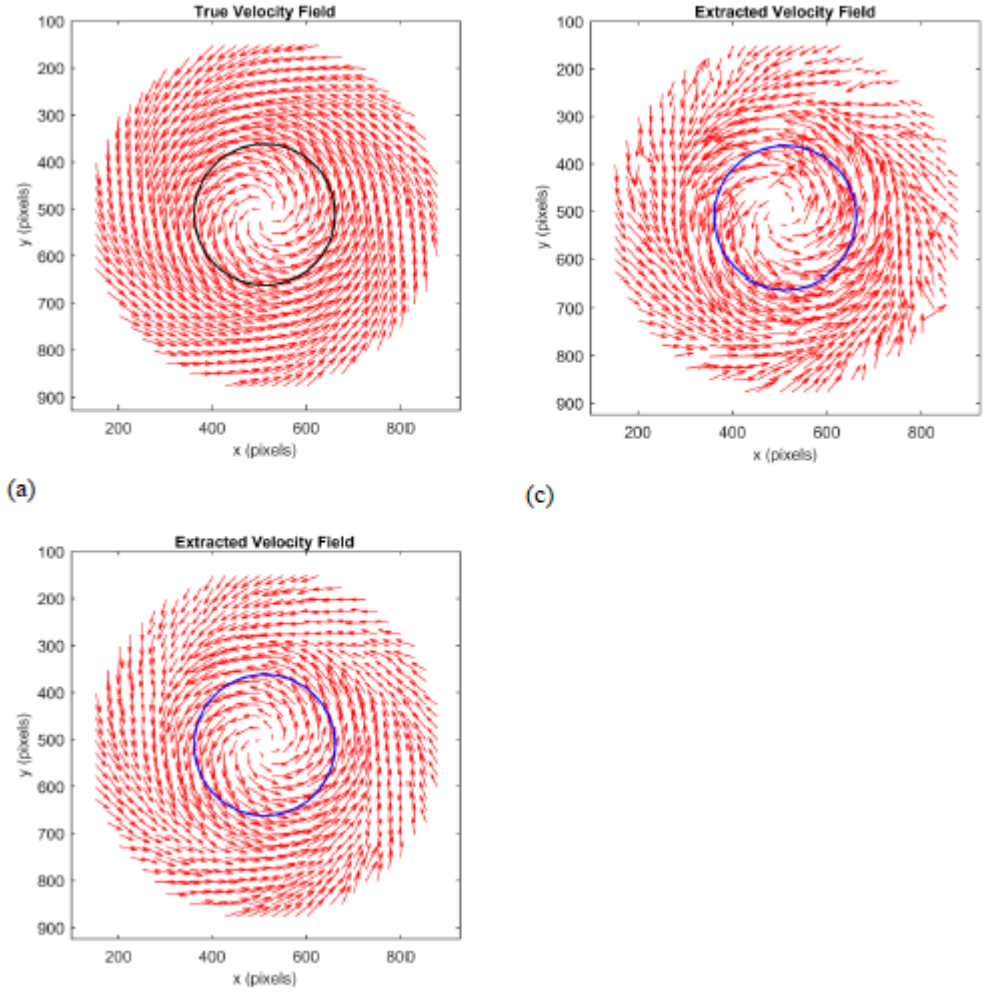

Figure 3. Velocity vectors: (a) true field, (b) extracted field from clean images, and extracted field from noisy images.

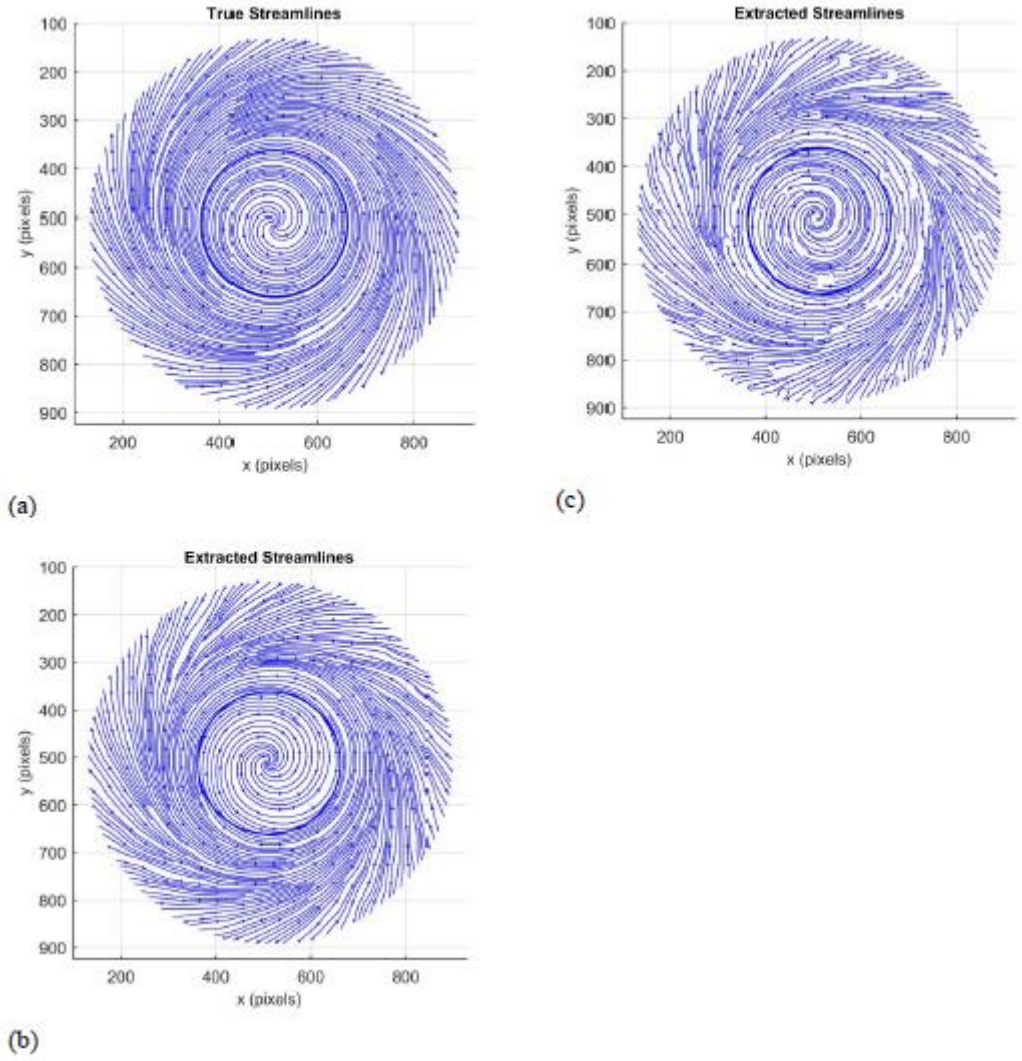

Figure 4. Streamlines: (a) true field, (b) extracted field from clean images, and (c) extracted field from noisy images.

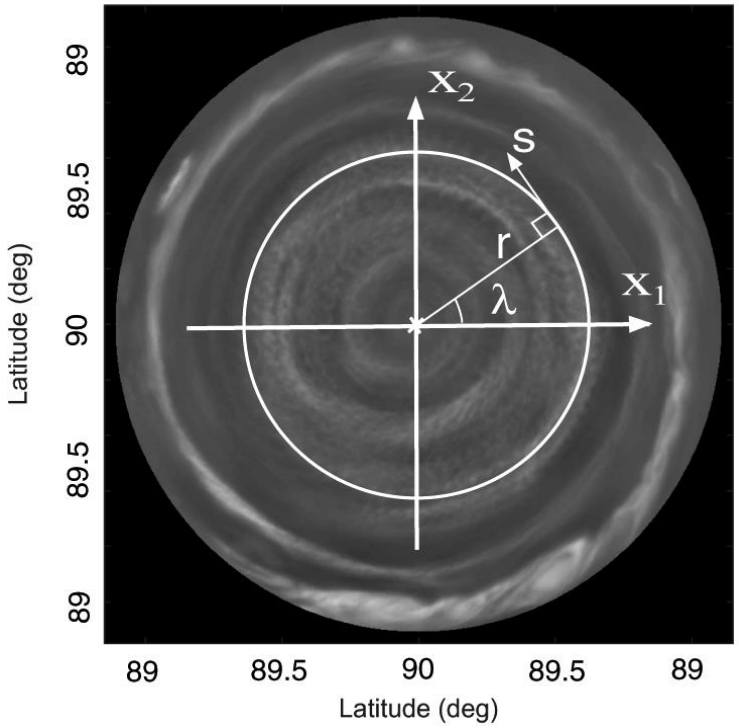

Figure 5. The image coordinate system overlaid on the time-averaged NP cloud image.

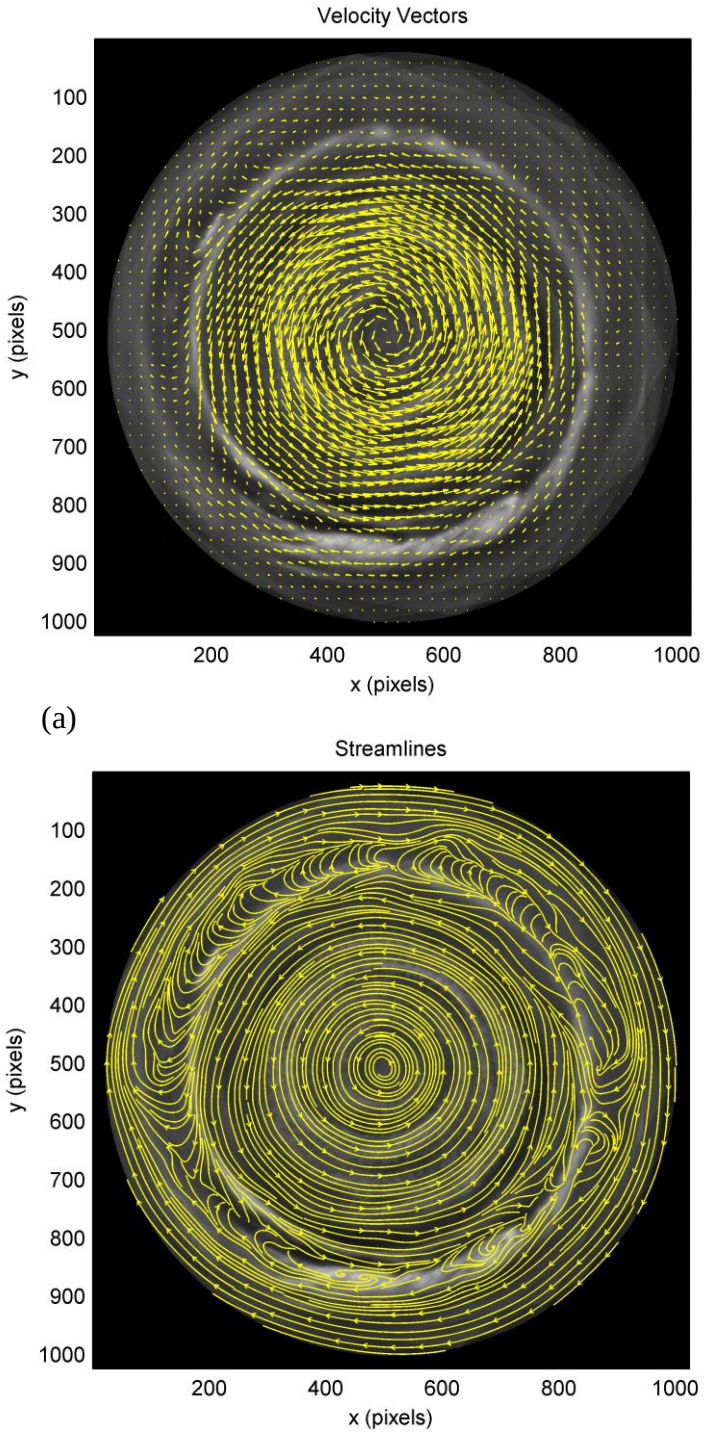

Figure 6. The time-averaged flow fields of Saturn's NPV before applying the rotational transformation for correction: (a) velocity vectors and (b) streamlines.

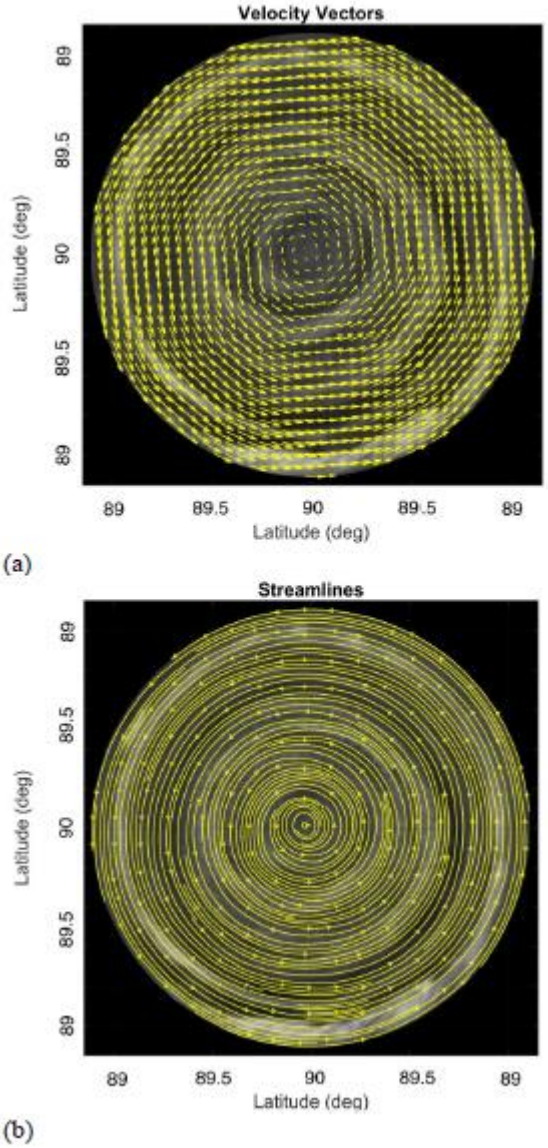

Figure 7. The time-averaged flow fields of Saturn's NPV after applying the inverse rotational transformation for correction: (a) velocity vectors and (b) streamlines.

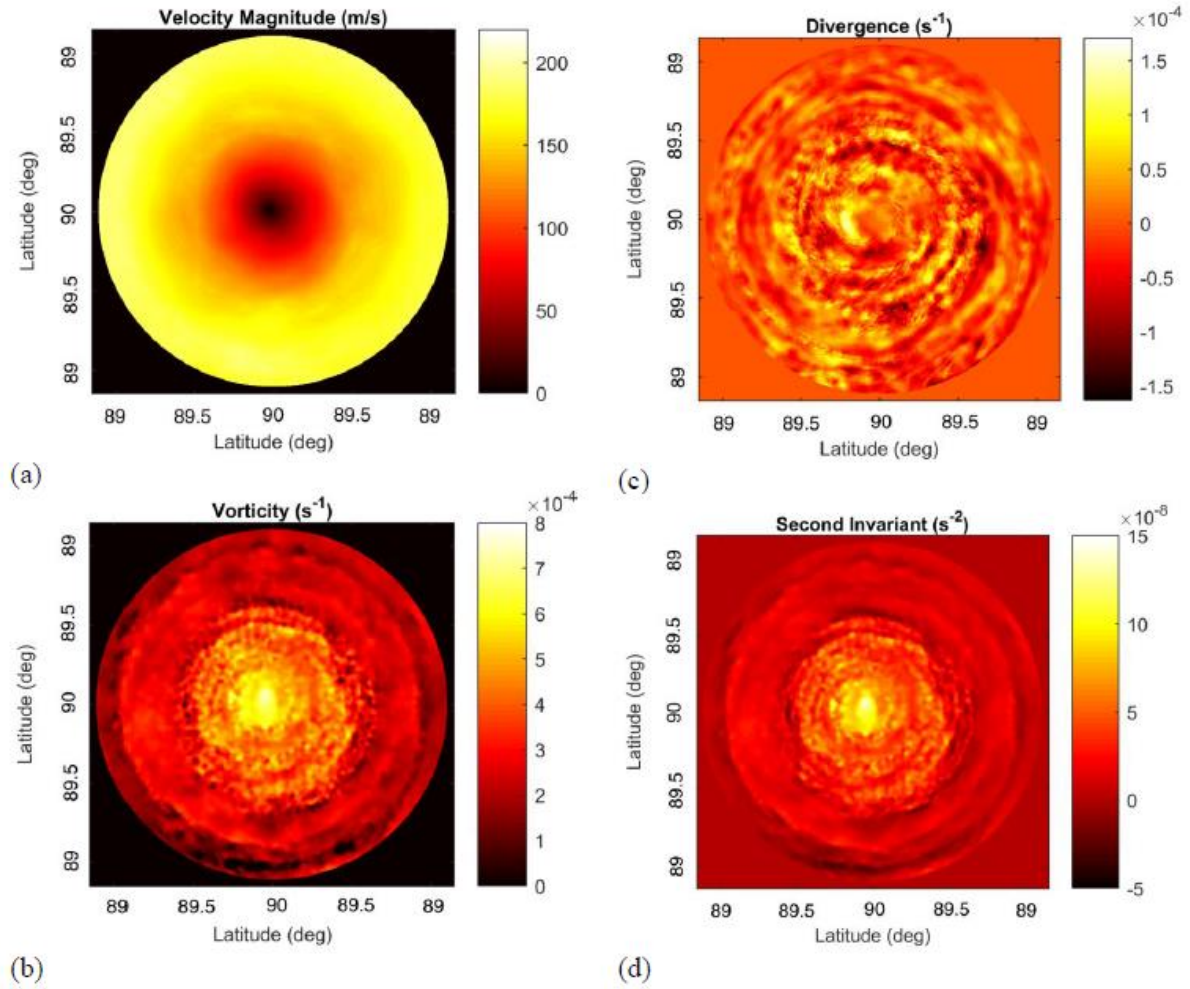

Figure 8. The time-averaged fields of the NPV: (a) the velocity magnitude, (b) the relative vorticity, (c) the divergence, and (d) the second invariant.

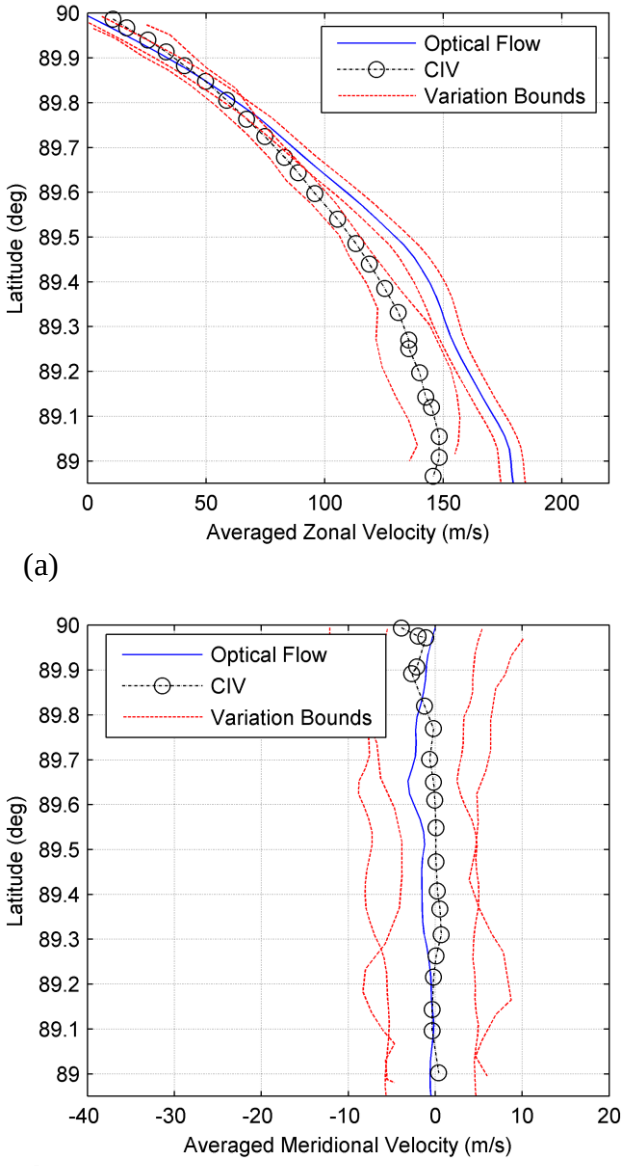

Figure 9. The mean profiles of the NPV: (a) the zonal (circumferential) velocity and (b) the meridional velocity.

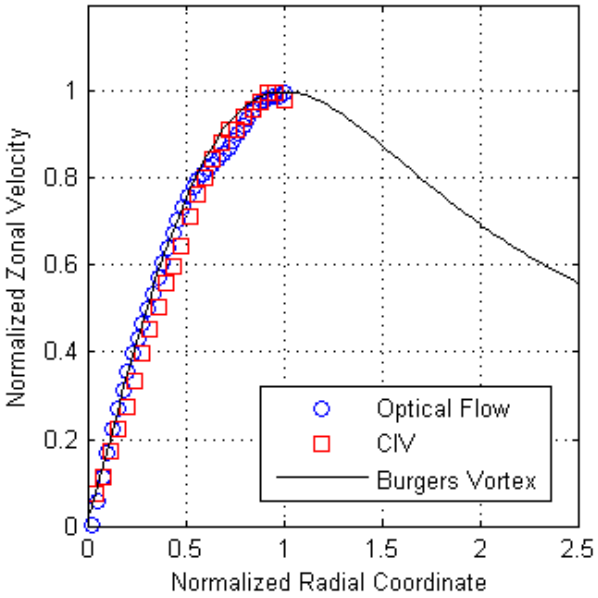

Figure 10. The normalized zonal velocity profiles of the NPV in comparison with the Burgers vortex model.

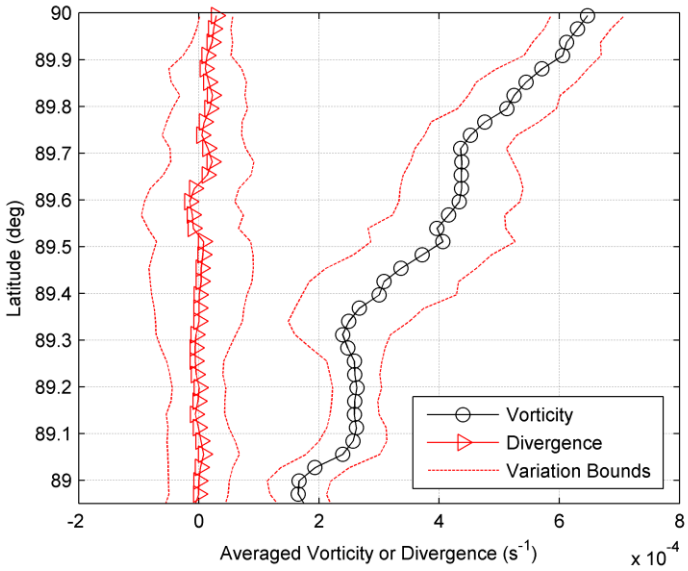

(a)

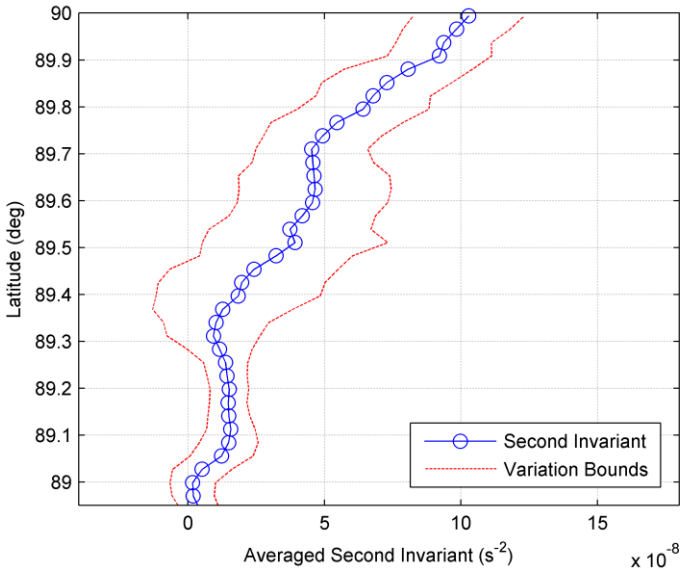

(b)

Figure 11. The mean profiles of the NPV: (a) the vorticity and divergence, and (b) the second invariant.

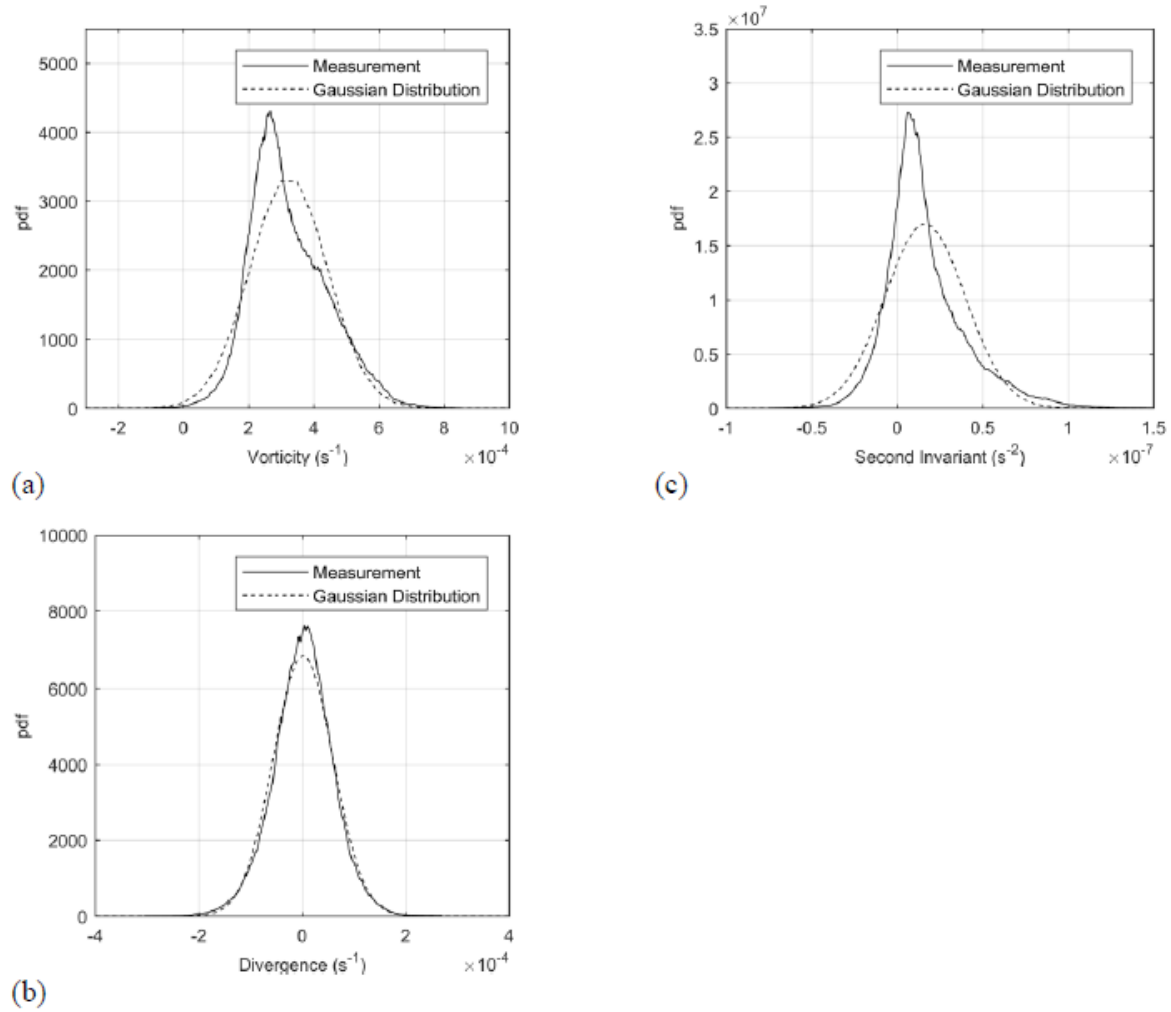

Figure 12. The probability density functions (pdfs): (a) the vorticity, (b) divergence, and (c) the second invariant.

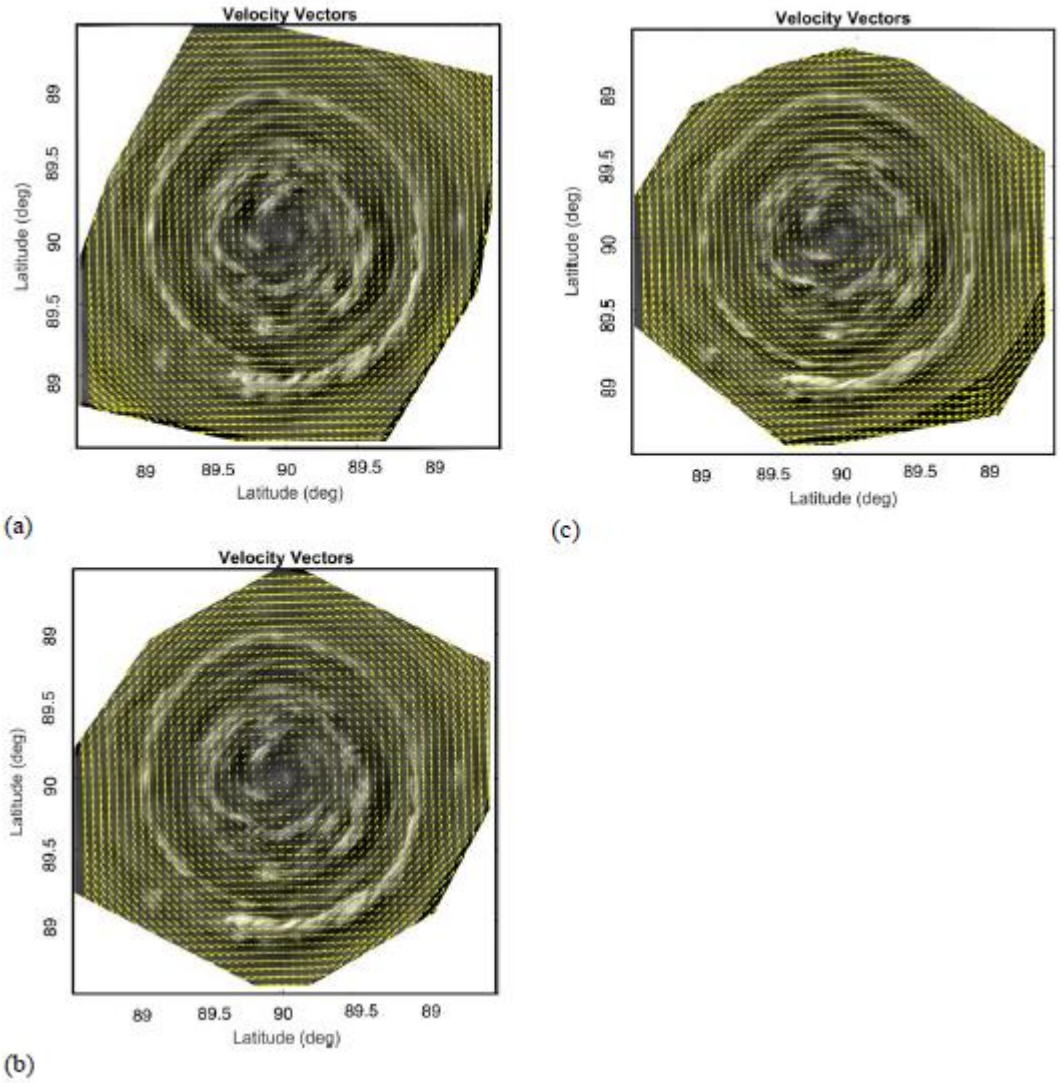

Figure 13. The velocity vectors in the first three instantaneous fields.

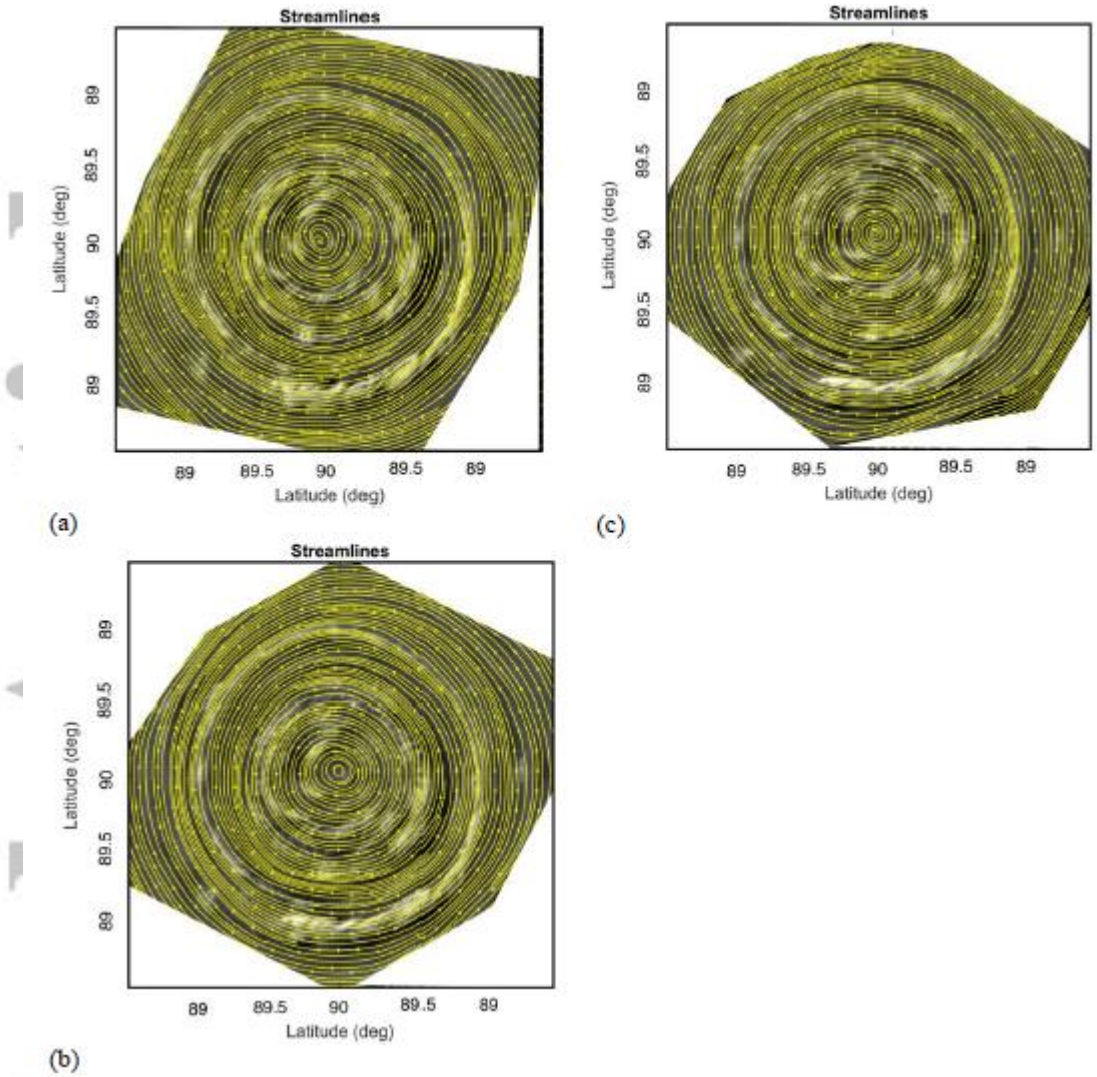

Figure 14. The streamlines in the first three instantaneous fields.

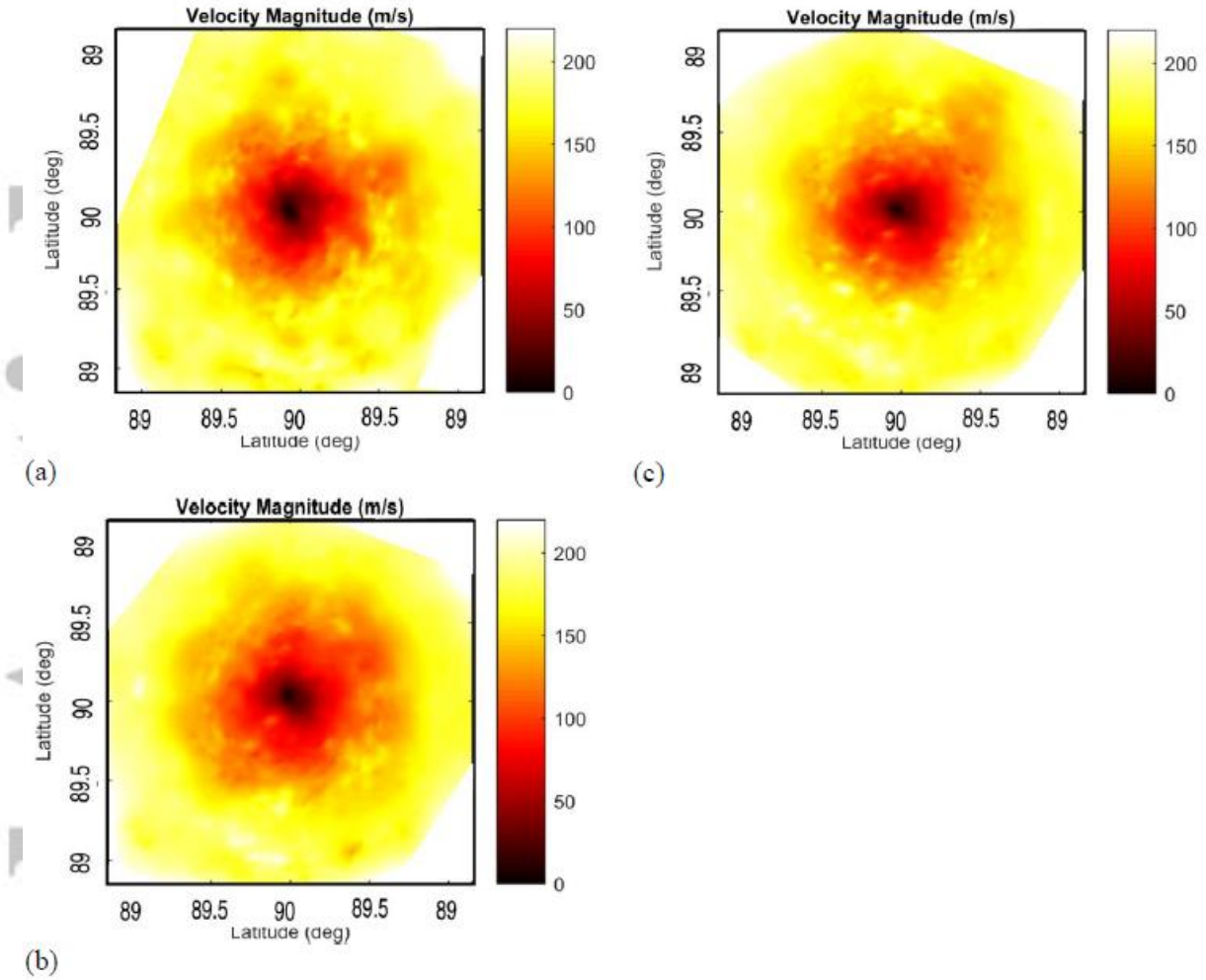

Figure 15. The first three instantaneous velocity magnitude fields.

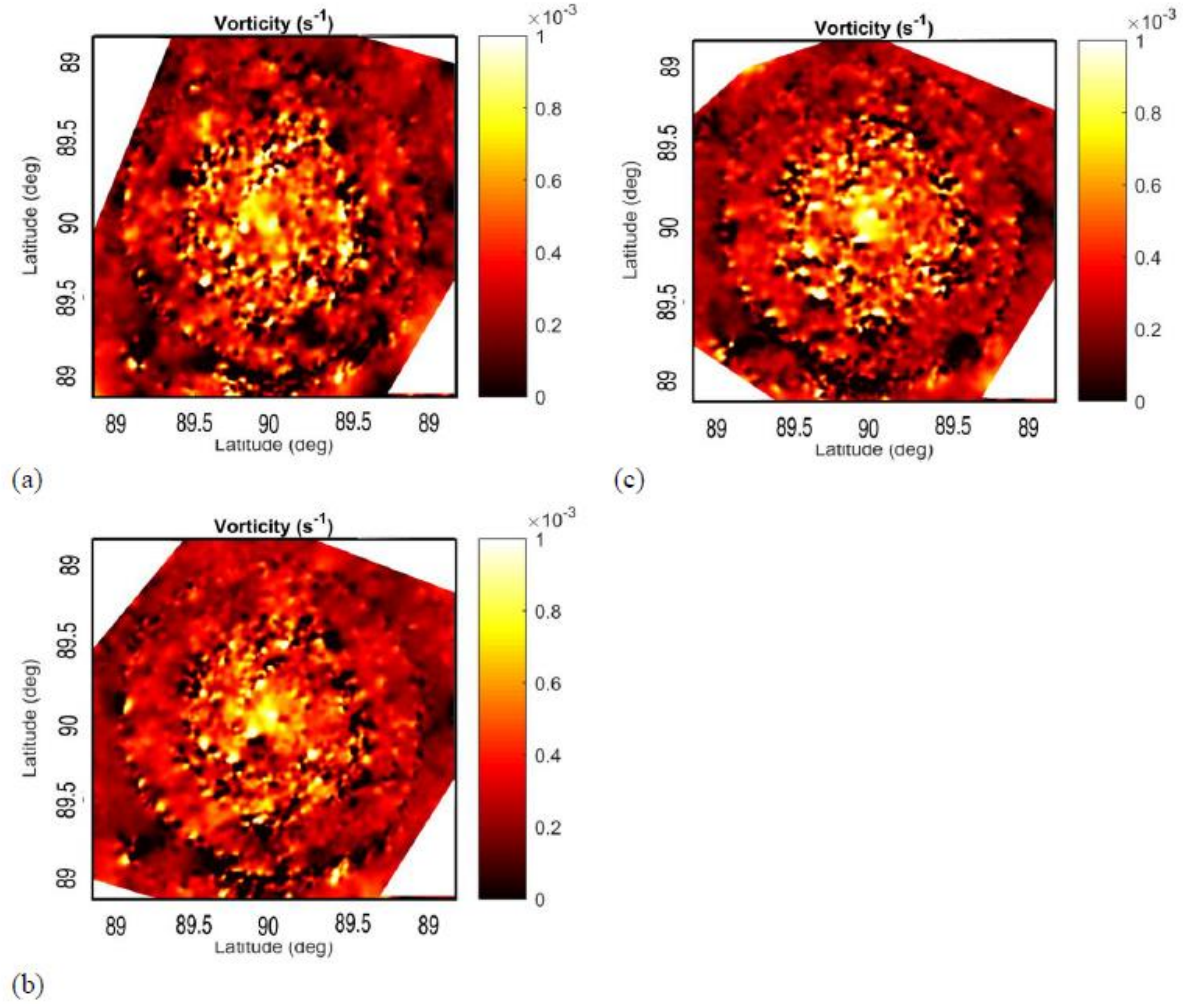

Figure 16. The first three instantaneous vorticity fields.

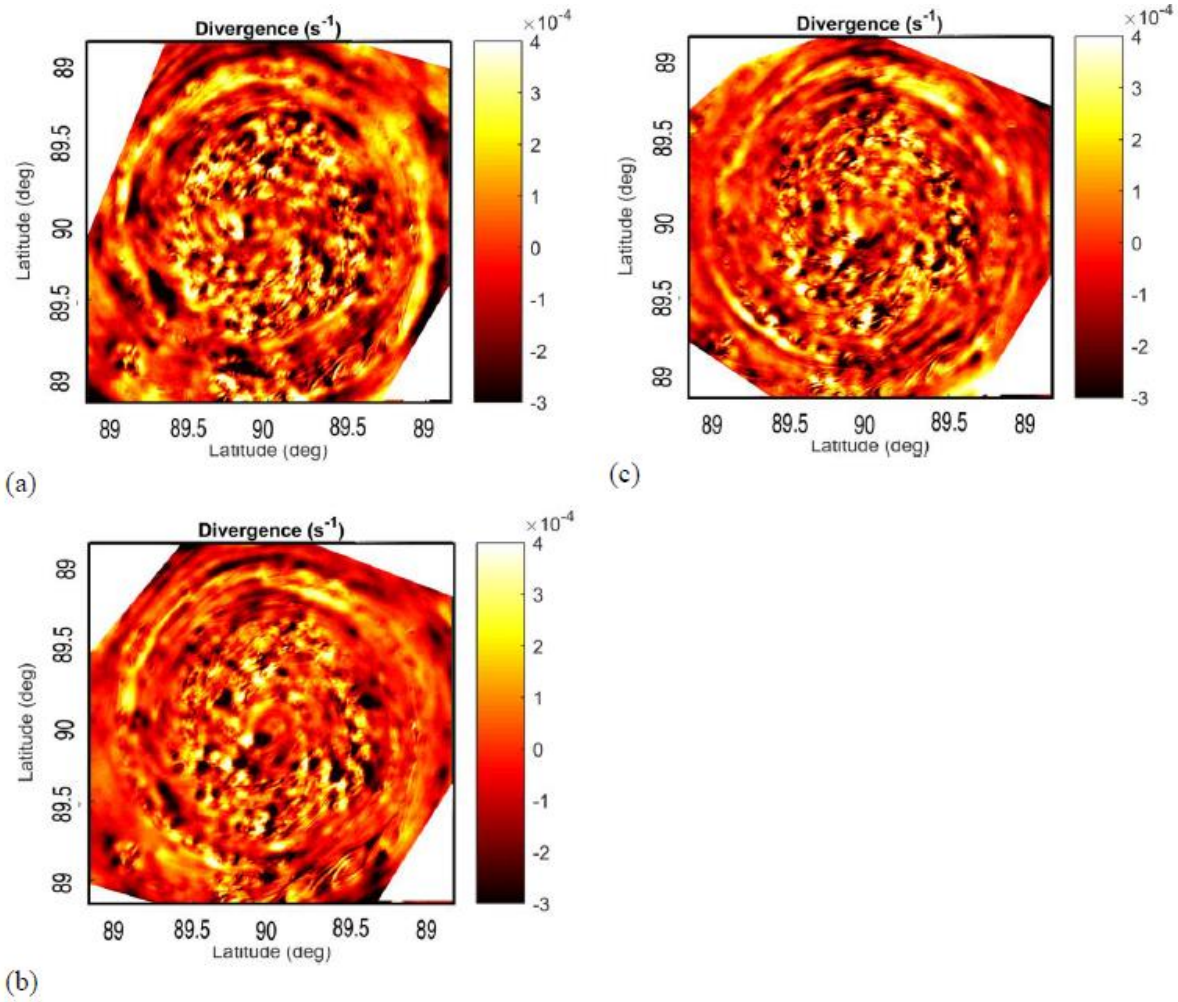

Figure 17. The first three instantaneous divergence fields.

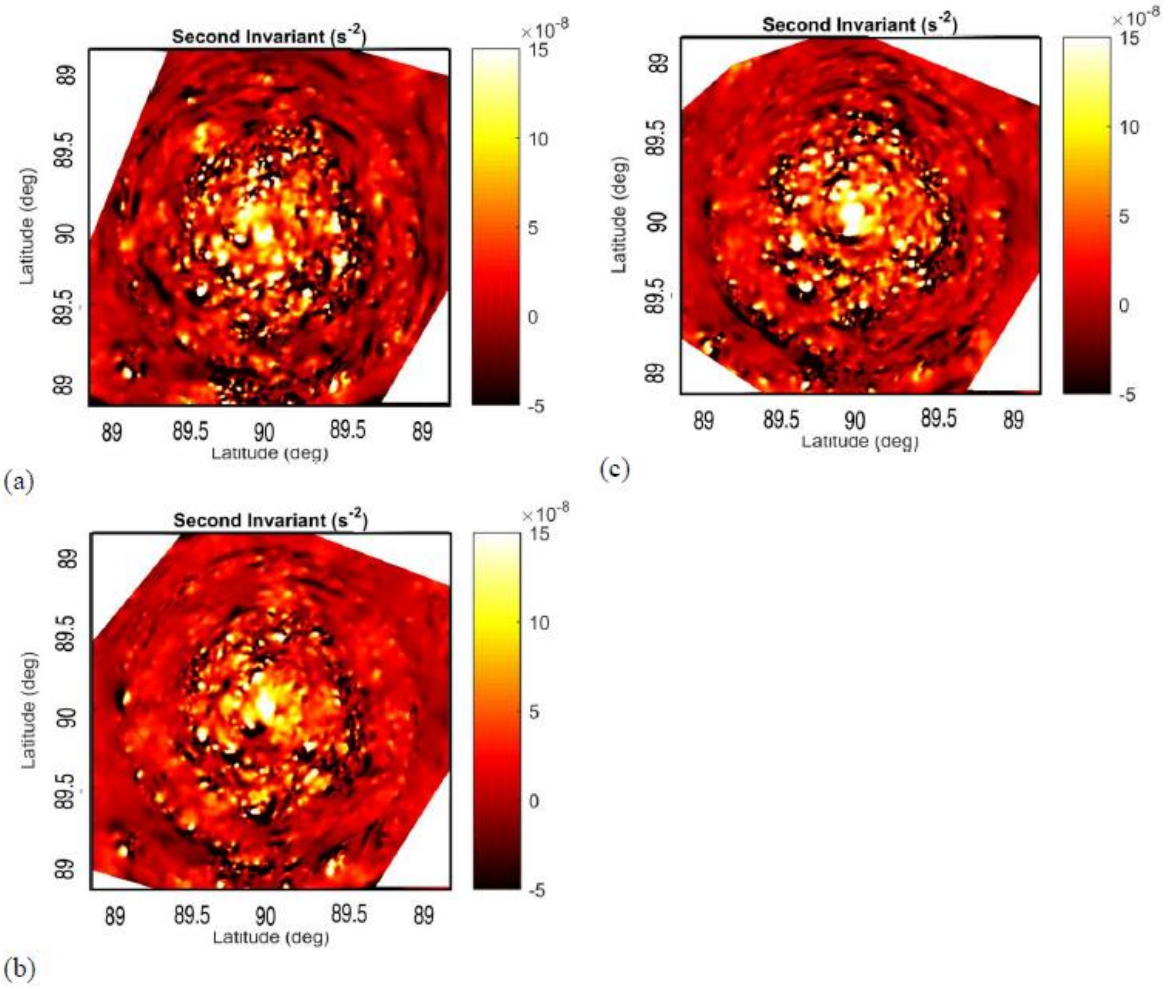

Figure 18. The first three instantaneous second invariant fields.

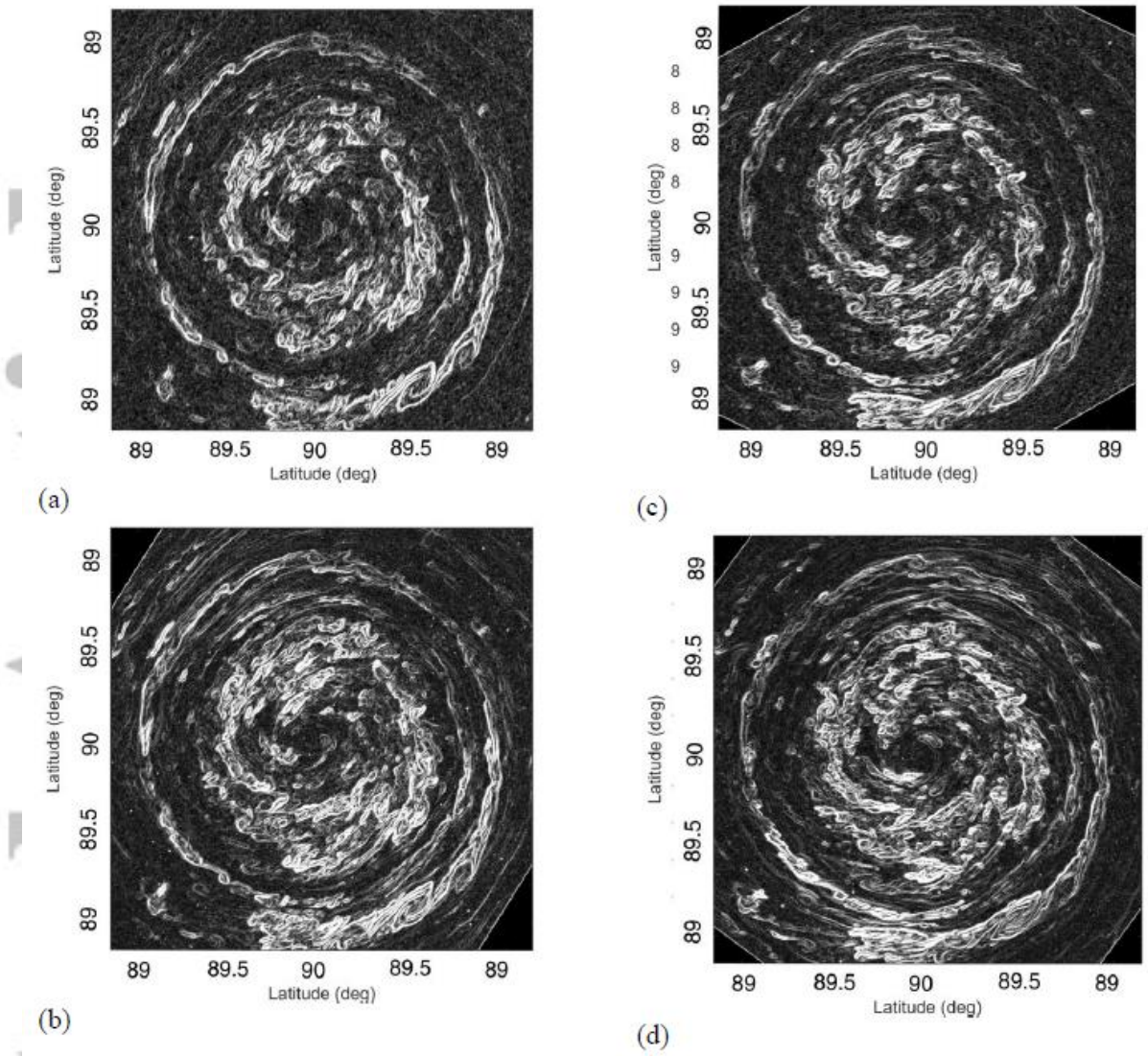

Figure 19. The first four intensity gradient magnitude fields of the cloud images of Saturn's north pole (NP) region, where the time intervals between the sequential image pairs are 21.9, 28.4, 20.5, and 28.0 min, respectively.

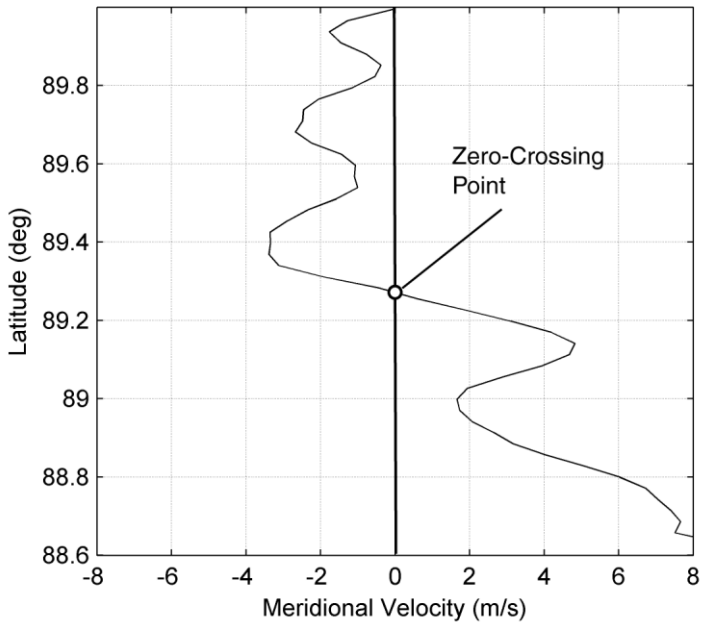

Figure 20. The profiles of the meridional velocity averaged from the first three instantaneous fields.

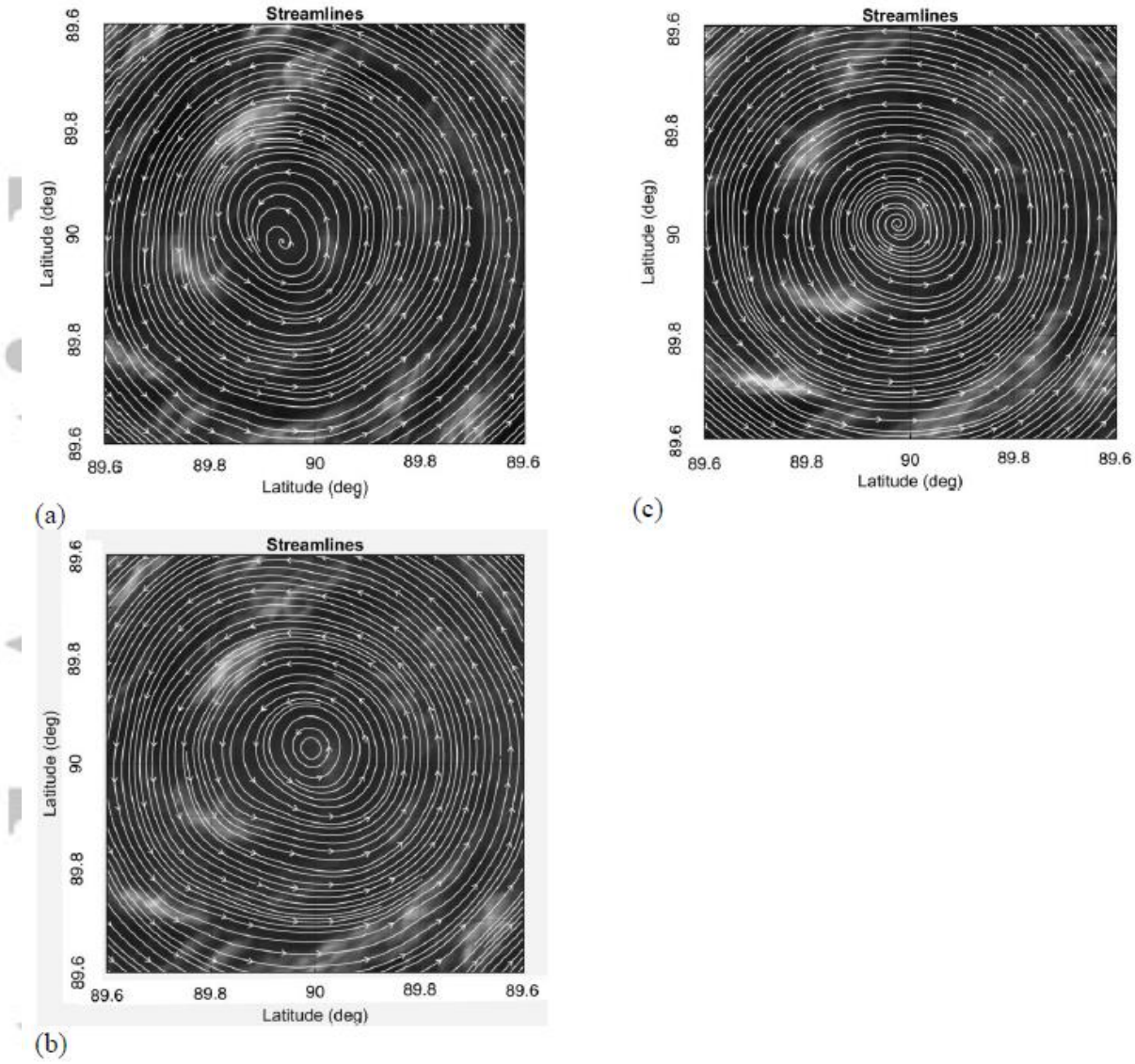

Figure 21. Zoomed-in instantaneous patterns of streamlines near the NP, (a) first instantaneous field, (b) second instantaneous field, and (c) third instantaneous field.

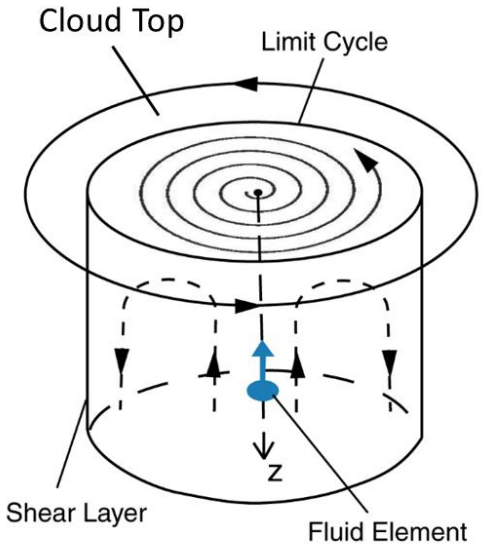

Figure 22. Conjectured flow structure ossssf the NPV.